Modeled Three-Dimensional Currents and Eddies on an Alongshore-Variable Barred Beach

Christine M. Baker[1], Melissa Moulton[2], Britt Raubenheimer[3], Steve Elgar[3], and Nirnimesh Kumar[1]

[1]Department of Civil & Environmental Engineering, University of Washington, Seattle, WA

[2]Applied Physics Laboratory, University of Washington, Seattle, WA

[3]Woods Hole Oceanographic Institution, Woods Hole, MA

Key Points:

- Trends in SWASH-simulated nearshore circulation patterns and magnitudes on an alongshore-variable barred beach are similar to observations
- Small length-scale eddies are intensified by wave directional spread, and large eddies are enhanced by alongshore bathymetric variability
- Eddy length scales and low-frequency currents are weakly vertically-dependent in the outer surf zone and depth-uniform in shallower water

Corresponding author: Christine Baker, Ph# 206-221-7623,cmbaker9@uw.edu

Abstract

Circulation in the nearshore region, which is critical for material transport along the coast and between the surf zone and the inner shelf, includes strong vortical motions. The horizontal length scales and vertical structure associated with vortical motions are not well documented on alongshore-variable beaches. Here, a three-dimensional phase-resolving numerical model, Simulating WAves till SHore (SWASH), is compared with surfzone waves and flows on a barred beach, and is used to investigate surfzone eddies. Model simulations with measured bathymetry reproduce trends in the mean surfzone circulation patterns, including alongshore currents and rip current circulation cells observed for offshore wave heights from 0.5 to 2.0 m and incident wave directions from 0 to 15° relative to shore normal. The length scales of simulated eddies, quantified using the alongshore wavenumber spectra of vertical vorticity, suggest that increasing wave directional spread intensifies small-scale eddies ($O(10)$ m). Simulations with bathymetric variability ranging from alongshore uniform to highly alongshore variable indicate that large-scale eddies ($O(100)$ m) may be enhanced by surfzone bathymetric variability, whereas small-scale eddies ($O(10)$ m) are less dependent on bathymetric variability. The simulated vertical dependence of the magnitude and mean length scale (centroid) of the alongshore wavenumber spectra of vertical vorticity and very low-frequency ($f \approx 0.005$ Hz) currents is weak in the outer surf zone, and decreases toward the shoreline. The vertical dependence in the simulations may be affected by the vertical structure of turbulence, mean shear, and bottom boundary layer dynamics.

Plain Language Summary

The nearshore region includes the surf zone, where waves break, and the inner shelf, which extends several km offshore from the surf zone. Within this region, currents transport contaminants, sediments, and larvae along the coast and between the beach and the shelf. Nearshore eddies are rotational currents that fluctuate at timescales longer than individual waves and shorter than mean hourly currents, and are important to mixing and transport. Here, a three-dimensional numerical model simulates observed waves and flow patterns on a natural beach near Duck, NC with highly variable seafloor elevations (*e.g.,* bumps and holes). Estimates of the alongshore (parallel to the coastline) length of simulated eddies suggest that large eddies are enhanced by higher variability in the seafloor, whereas the intensity of small eddies increases when waves enter the surf zone with larger directional spread (from multiple direc-

tions). The structure and strength of nearshore eddies over the water column is shown to vary across the surf zone.

1 Introduction

The nearshore region consists of the surf zone, extending from the shoreline to the seaward limit of depth-induced wave breaking, and the inner shelf, a region with overlapping surface and bottom boundary layers on the continental shelf offshore of the surf zone [*Lentz and Fewings*, 2012]. Quantifying circulation dynamics and the transport of material (*e.g.,* contaminants, sediments, and larvae) in the nearshore is critical given the concentration of recreational, commercial, and ecosystem resources in this region [*Boehm et al.*, 2017]. Nearshore currents may dilute or concentrate pollutants and pathogens that cause gastrointestinal infections and require beach closures [*Stoner and Dorfman*, 2007], and excess nutrient supply from terrestrial runoff may lead to eutrophication in coastal zones, creating hypoxic conditions that threaten benthic organisms and ecosystem health [*Boehm et al.*, 2016]. In addition, species inhabiting the nearshore (*e.g.,* intertidal invertebrate gametes) exploit cross-shore circulation for recruitment and settlement [*Pineda et al.*, 2007; *Shanks et al.*, 2010]. A comprehensive understanding of nearshore dynamics is necessary to maintain public safety and reduce anthropogenic stresses on ecosystems.

Surfzone circulation is the result of complex interactions between surface waves, bathymetric irregularities, and bottom boundary layer dynamics. Mean cross-shore velocities are characterized by a balance between radiation-stress gradients, barotropic-pressure gradients, and a weaker contribution from bottom stress, resulting in wave setup and an offshore near-bed return current [*i.e.,* 'undertow', *Longuet-Higgins and Stewart*, 1964; *Bowen et al.*, 1968; *Stive and Wind*, 1982; *Raubenheimer et al.*, 2001]. Wave-induced mean alongshore currents result from alongshore barotropic-pressure gradients [*Apotsos et al.*, 2008; *Hansen et al.*, 2015] and cross-shore gradients of the off-diagonal component of the radiation-stress tensor [*Longuet-Higgins*, 1970; *Feddersen et al.*, 1998; *Garcez-Faria et al.*, 1998], primarily balanced by bottom stress [*Visser*, 1986; *Simons et al.*, 1992; *Reniers et al.*, 2004a]. Wave breaking over alongshore bathymetric variations drives rip currents and meandering alongshore currents, including cell-like circulation patterns [*MacMahan et al.*, 2006; *Dalrymple et al.*, 2011; *Castelle et al.*, 2016; *Moulton et al.*, 2017].

The vertical structure of surfzone currents depends on the forces associated with surface wave breaking, bottom friction, and interaction with the three-dimensional circulation [*Putrevu et al.*, 1995; *MacMahan et al.*, 2004], and is altered by the vertical distribution of turbulence in the water column, which depends on the breaking wave energy and bed roughness [*Feddersen and Trowbridge*, 2005; *Feddersen*, 2012; *Henderson et al.*, 2017]. Field and numerical modeling studies have investigated the vertical profile of undertow [*Garcez-Faria et al.*, 1998] and of mean alongshore currents [*Garcez-Faria et al.*, 2000; *Reniers et al.*, 2004a]. However, the three-dimensional structure of surfzone velocities at timescales longer than those of wind waves (*e.g.,* surfzone eddies) and their implications for material exchange are not understood well.

Surfzone eddy activity contributes to dispersion and mixing, thus affecting the transport of material along the coast and between the surf zone and the inner shelf [*Spydell and Feddersen*, 2009; *Clark et al.*, 2010, 2011; *Suanda and Feddersen*, 2015]. Very low-frequency (VLF) vortical motions at timescales greater than 250 s (approximately $f < 0.004$ Hz, where f is frequency), longer than infragravity timescales ($0.004 < f < 0.040$ Hz), may be generated by shear instabilities [*Bowen and Holman*, 1989; *Oltman-Shay et al.*, 1989; *Allen et al.*, 1996] and wave-breaking induced vorticity [*Peregrine*, 1998; *Haller et al.*, 1999]. Shear instabilities in an obliquely incident wave-driven alongshore current have been observed with length scales up to several hundred meters [*Oltman-Shay et al.*, 1989]. Wave-group driven alongshore radiation stress gradients from alongshore wave-breaking variability may contribute to surfzone eddy generation with length scales on the order (O) of 100 m [*Haller et al.*, 1999; *Reniers et al.*, 2004b; *Long and Özkan Haller*, 2009]. As a result of alongshore gradients in wave dissipation, short-crested breaking waves generate vorticity with length scales $O(10)$ m [*Peregrine*, 1998; *Clark et al.*, 2012], which are hypothesized to coalesce to larger scales $O(100)$ m due to an inverse energy cascade [*Kraichnan*, 1967; *Spydell and Feddersen*, 2009; *Boffetta and Ecke*, 2012; *Elgar and Raubenheimer*, 2020]. The length scales associated with vortical motions generated by both shear instabilities and wave breaking have been explored for depth-integrated velocities on alongshore-uniform beaches [*Spydell and Feddersen*, 2009; *Feddersen et al.*, 2011; *Feddersen*, 2014; *Kumar and Feddersen*, 2017] and an alongshore-varying beach [*O'Dea et al.*, 2020], but have not been explored for depth-varying velocities on beaches with complex bathymetry.

Surfzone vortical motions, often assumed to be depth-uniform, usually have been measured at a single elevation with a horizontally spaced sensor array. However, two recent stud-

ies on a barred beach measured low-frequency motions with vertically stacked electromagnetic current sensors [*Lippmann et al.*, 2016] and acoustic Doppler profilers [*Henderson et al.*, 2017]. These studies found that low-frequency cross- and alongshore velocities are weakly vertically dependent in the outer surf zone [*Lippmann et al.*, 2016; *Henderson et al.*, 2017]. Analytic solutions based on bottom boundary layer theory include complex vertical structure of low-frequency motions in the presence of a horizontally sheared alongshore current [*Lippmann and Bowen*, 2016]. Although these studies have established that eddies in the outer surf zone have some vertical variability, further investigation is necessary to understand the vertical dependence of VLF currents for varying beach profiles and wave conditions.

Numerical modeling has been used to investigate the three-dimensionality of surfzone vortical motions. Phase-averaged models, which simulate the evolution of the wave energy spectrum, are skillful at reproducing wave-induced dynamics, including rip-current circulation, alongshore currents, and wave setup [*Reniers et al.*, 2004a; *Uchiyama et al.*, 2010; *Kumar et al.*, 2012]. Studies using three-dimensional phase-averaged model simulations indicate that vertical shear instabilities modify depth-dependent currents due to dispersive mixing [*Newberger and Allen*, 2007a,b], and that VLF motions are excited on complex bathymetry [*Uchiyama et al.*, 2017]. However, the parameterizations of wave-induced vorticity associated with energy dissipation from short-crested wave breaking used in phase-averaged models have not been tested extensively.

Coupled ocean-circulation and phase-averaged wave models (*e.g.,* COAWST) simulate vertically varying surfzone circulation [*Warner et al.*, 2010; *Kumar et al.*, 2012], and can be one-way coupled with depth-averaged phase-resolving models (*e.g.,* funwaveC) to allow for the investigation of three-dimensional eddies resulting from bulk vorticity injection similar to that resulting from short-crested wave breaking [*Kumar and Feddersen*, 2017]. However, wave-forced rotational flows associated with eddies may be aliased as a result of smaller time steps in the phase-resolving simulations [*Kumar and Feddersen*, 2017]. In addition, two-way coupled wave-current interactions between three-dimensional eddies and propagating waves are not included.

Phase-resolving Boussinesq models (*e.g.,* FUNWAVE-TVD and funwaveC), which simulate individual wave propagation, have been used to study surfzone vorticity dynamics, including finite-crested wave-breaking eddy generation [*Feddersen*, 2014; *Hally-Rosendahl and Feddersen*, 2016]. These models are depth integrated, and thus do not resolve eddy

vertical variability. Three-dimensional phase-resolving non-hydrostatic numerical models, such as Simulating WAves til SHore (SWASH) and NHWAVE, contain the physics needed to simulate three-dimensional circulation and vorticity dynamics, including wave-forced eddy generation [*Zijlema et al.*, 2011; *Derakhti et al.*, 2016]. SWASH has been used to study nearshore wave breaking, infragravity wave dynamics, nonlinear infragravity-wave interactions, run-up oscillations, and nonlinear wave-dynamics [*Rijnsdorp et al.*, 2012, 2014; *Smit et al.*, 2013; *Ruju et al.*, 2014; *Smit et al.*, 2014; *de Bakker et al.*, 2016]. Although SWASH has skill simulating wave-induced flows measured in the laboratory, including the undertow profile and alongshore currents [*Rijnsdorp et al.*, 2017], the accuracy of SWASH-simulated surfzone circulation on an alongshore-variable beach has not been tested.

Here, SWASH is used to simulate three-dimensional wave propagation and circulation on a beach with complex alongshore-varying bathymetry. The field experiment and model setup are described in section 2, and the results comparing the observed with the simulated wave statistics and circulation patterns are presented in section 3. Additionally, the relative roles of alongshore bathymetric variability and directional spread in the horizontal and depth variability of length scales of the simulated eddies, and of the vertical structure of VLF horizontal velocities, are presented in section 3. The physical processes influencing the horizontal and depth variability of surfzone eddies and VLF currents are discussed in section 4. The results are summarized in section 5.

2 Methods

2.1 Field Experiment

Field observations were collected on an alongshore-inhomogeneous barred beach near Duck, North Carolina at the United States Army Corps of Engineers Field Research Facility (FRF, http://frf.usace.army.mil/frf.shtml) as part of the BathyDuck-2015 Experiment, a large effort to evaluate and improve the estimation of surfzone bathymetry [*Smith et al.*, 2017]. Instruments included offshore wave sensors in water depths (h) of 11 (x, y = 1295, 978 m, positive offshore and to the north, respectively) and 6 m (x, y = 606, 937 m) and an array of colocated pressure sensors and acoustic Doppler velocimeters (ADVs) in the surf zone, sampled at 2 Hz (Figure 1a,b). Two cross-shore transects of four colocated ADVs and pressure sensors were deployed from $-3.5 < z < -1.5$ m (positive upward and referenced to the NAVD88 datum, approximately local mean sea level), initially positioned 0.5 to 1.0 m above

the bed, and separated by approximately 125 m in the cross-shore and 75 m in the alongshore (Figure 1, red circles, y = 741 and 813 m). Two additional sensors were deployed south of these arrays near the FRF pier (y = 521 m). Occasionally, current meter data were omitted when sensors were out of the water (low tide) or buried (accretion).

Bathymetric surveys were performed on Oct. 14 and Nov. 16, 2015 with the Lighter Amphibious Resupply Cargo (LARC) vehicle using a single-beam acoustic sonar and RTK GPS (Figure 1). The survey data were smoothed to an 8-m cross-shore by 45-m alongshore gridded bathymetry with estimated root-mean-square vertical elevation errors of approximately 0.05 m, attributed to sampling and interpolation errors [*Plant et al.*, 2002; *Smith et al.*, 2017]. The surveys covered 1200-m in the alongshore (y = -100–1100 m) and spanned from the beach to $h \approx 9$ m (x = 50–950 m).

Between the most offshore position of the shoreline ($x = 135$ m) and the bar crest ($x = 235$ m), the Oct. 14 bathymetry has a maximum surfzone alongshore standard deviation ($\sigma_{y,sz}$) of 0.86 m (Figure 1c, left vertical bar, S3a) located in the trough region. The nondimensional metric of bathymetric nonuniformity, the spatially averaged and normalized squared difference between the measured depth ($h(x, y)$) and the alongshore-averaged cross-shore depth ($\overline{h}(x)$) [*Ruessink et al.*, 2001] is defined as:

$$\chi^2 = \frac{1}{L_x L_y} \int_{x_0}^{x_{sz}} \int_{y_{\text{south}}}^{y_{\text{north}}} \left(\frac{h(x,y) - \overline{h}(x)}{\overline{h}(x)} \right)^2 dy dx \tag{1}$$

where L_x and L_y are the cross-shore and alongshore length where χ^2 is evaluated. χ^2 computed from x = 134 m (the farthest offshore extent where h = 0 m, x_0) to x = 260 m (the edge of the surf zone for the simulations with the largest wave simulation, x_{sz}) and $-100 \geq y \geq 1100$ m is 0.099. On Oct. 14 (Nov. 16), the average shoreline position was approximately x = 108 m (110 m), and a single bar was located near x = 235 m (215 m) with an alongshore-variable trough near x = 175 m (170 m). In both bathymetric surveys, the morphology includes bar-trough patterns (*e.g.,* Figure 1a: y = 600–750 m, Figure 1b: y = 550–700 m), variable terraces (*e.g.,* Figure 1a: y = 750–825 m, Figure 1b: y = 700–800 m), and a scoured channel under the FRF pier (Figure 1a,b: y = 500 m). Between Oct. 14 and Nov. 16, there was on average about a 10 m shoreward migration of the bar crest at y = 600–1100 m and a southward migration of some bathymetric features, such as the depression from $y = 600-750$ m on Oct. 14, which may have migrated to $y = 550 - 700$ by Nov. 16 (Figure 1a,b).

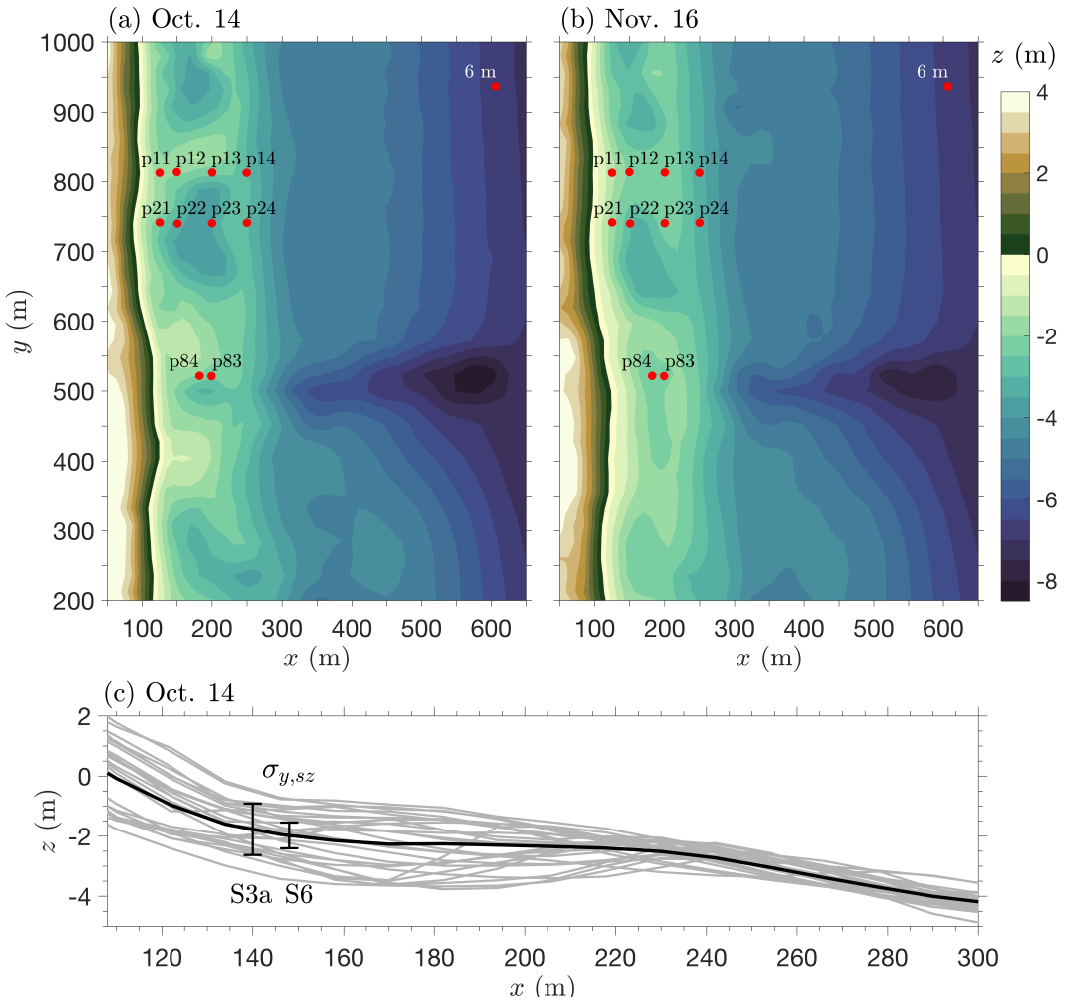

Figure 1. Locations of colocated ADVs and pressure gauges (red symbols) and bathymetry (z, color contours, scale on the right) measured on (a) Oct. 14, 2015 and (b) Nov. 16, 2015 versus cross- (x) and alongshore (y) coordinates. Bathymetry from Oct. and Nov. have alongshore-varying sandbar-trough and terrace systems interrupted by channels. The deep channel at around y = 500 m is formed from scour near the FRF pier. (c) Vertical elevation (z) versus cross-shore coordinate (x) for profiles every 45 m in the alongshore (S3a, gray curves) and the alongshore-averaged profile (S7, black curve) for Oct 14. The alongshore standard deviation of the bathymetry ($\sigma_{y,sz}$) in the surf zone is denoted with vertical bars for simulations S3a and S6 (Tables 1, 2).

ADV measurements were quality controlled [*Elgar et al.*, 2005] and used to compute hourly bulk current and wave parameters, reported as the average of six 512-second data collections each hour. A frequency-dependent correction for depth using linear wave theory was applied to nearshore pressure measurements to estimate sea-surface elevation statistics [*Guza and Thornton*, 1980]. Significant wave heights (H_s, 4 times the standard deviation of sea-surface elevation fluctuations for $0.05 < f < 0.30$ Hz) have an estimated error $< 5\%$. The energy-weighted wave angles (θ) and directional spread (σ_θ) were computed for the same frequency range using directional moments [*Kuik et al.*, 1988], and have an estimated error of 5° owing to compass inaccuracies. Incident waves from counter-clockwise (from the north-east) and clockwise (from the south-east) of shore-normal are reported as $\theta > 0°$ and $\theta < 0°$, respectively. The range of the mean water level ($\langle\eta\rangle$, including tides, surge, and other large-scale water-level fluctuations) measured by a NOAA tide gauge ($h = 6$ m, $x, y =$ 582, 509 m) varied from -0.6 to 1.0 m. In 11-m water depth, H_s ranged from 0.3 to 2.0 m, θ varied from -45° to 50°, σ_θ was between 25° to 40°, and the peak wave periods (T_p) ranged from 4 to 12 s. In 2-m water depth, wave heights were depth limited, and thus varied tidally, wave directions usually were close to shore-normal, and directional spreads decreased relative to offshore waves. The maximum hourly-average current speeds at a nearshore sensor at $h \approx 2$ m ($x, y = 150, 740$ m), was approximately 0.5 m/s (0.6 m/s) in the cross-shore (alongshore) when $H_s > 1.5$ m.

2.2 Numerical Modeling Testing Framework

Nearshore circulation and wave propagation were simulated using Simulating WAves till SHore (SWASH), a three-dimensional open source non-hydrostatic wave-flow model [*Zijlema et al.*, 2011]. SWASH solves the nonlinear shallow water equations including non-hydrostatic pressure, and conserves temperature, salinity, and suspended sediment [*Zijlema and Stelling*, 2005]. The second-order finite difference approximations (in time and space) in SWASH improve the computational efficiency, while correcting for frequency dispersion through the addition of more vertical layers. The steepening wave front is resolved in simulations with sufficient vertical resolution and regarded as a jump-discontinuity in the flow variables (free surface, velocities). Conservation of momentum is enforced across the discontinuity, which enables an energy dissipation rate similar to a hydraulic jump [*Smit et al.*, 2013]. The hydrostatic front approximation that initiates wave breaking based on thresholds also is used in case the vertical gradients are not resolved adequately. Vertical mixing is ap-

proximated using a $k-\epsilon$ model, where k is the turbulent kinetic energy per unit mass and ϵ is the dissipation rate of turbulent kinetic energy per unit mass [*Launder and Spalding*, 1983]. The sensitivity to other approaches for vertical mixing is not explored here [*Rijnsdorp et al.*, 2017, see Appendix A for further details about the model].

SWASH was run on a 2-m-resolution horizontal grid spanning 1500 m alongshore and 900 m cross-shore from the shoreline to $h = 9$ m water depth with 5 vertical layers. Simulations were run with the observed bathymetry interpolated to the model grid with the still water level set to the hour-averaged observed ($h = 6$ m) water elevation ($\langle\eta\rangle$). To allow for north and south periodic boundary conditions, the domain was extended an additional 124 m alongshore on the northern and southern boundaries, converging exponentially to an alongshore-averaged bathymetry. All simulations were conducted for 2 hours with an initial time step of 0.04 seconds and a cycle length (repeated length of the time series realization) of 1 hr. After 1 hr of model spin up, 1-Hz output for the second hour is used for analysis. Further information about the numerical approach and model settings are provided in Appendix A.

The model was forced uniformly along the offshore boundary by a model-generated JONSWAP spectrum based on the observed offshore bulk wave parameters (H_s, T_p, θ, and σ_θ in $h = 11$ m) and a peakedness parameter (γ_J) calibrated to match the observed spectra ($\gamma_J = 1.4 - 1.9$). Errors introduced by applying forcing from an 11-m depth measurement at the 9-m depth model domain boundary are estimated to be small, with refraction resulting in differences of less than 1° in direction and less than 0.01 m in wave height. Bulk wave and current statistics from model simulations with bathymetry derived from the Oct. 14 survey (Figure 1a) are compared with observations for three directionally spread wave conditions (Table 1). Two of the simulations (S1 and S2, observed conditions on Oct 20 10:00 and 15:00 Eastern Daylight Time (EDT)) were selected to compare oblique with shore-normal waves during lower-energy conditions. The third simulation (S3a, observed conditions on Oct 28 00:00 EDT) has higher-energy, normally incident waves. Additionally, the sensitivity of the simulated nearshore circulation to bathymetry is investigated by repeating the third simulation (S3a) with bathymetry observed on Nov. 16 (S3b, Figure 1b). The surfzone width (L_{sz}) for each simulation is the distance from the alongshore-averaged shoreline position (x_{sl}, set by the mean water elevation) to the outer edge of the surf zone (x_{sz}, beginning of breaker zone), defined as the cross-shore location with the maximum cross-shore gradient in the alongshore-averaged significant wave height, $d\langle H_s\rangle_y/dx$ (Table 1).

The numerical framework and stability of SWASH impacted the selection of the test cases. For conditions with highly oblique, directionally spread waves ($\theta > 20°, \sigma_\theta > 30°$), unrealistic alongshore banding of H_s resulted from interference of the limited directional components that could be included in the domain geometry. Additionally, SWASH became unstable in the swash zone for moderate-energy oblique waves conditions ($\theta > 20°$, $H_s > 1$ m). Simulations were forced with a JONSWAP spectrum generated with the bulk wave parameters, and thus time periods with bi-modal wave spectra, including from Oct. 14 10:00 to Oct. 17 23:00 EDT, were not simulated. The stability was compromised and computational time substantially increased when the number of vertical layers was doubled.

Table 1. Simulated test cases forced with observed conditions, including hour-average mean water elevation ($\langle\eta\rangle$) and offshore (h = 11 m) significant wave height (H_s), peak wave period (T_p), incident wave angle ($\theta = 0°$ is shore-normal, $\theta < 0°$ indicates waves from the southeast), directional spread (σ_θ), and the JONSWAP gamma parameter (γ_J). Model bathymetry for each simulation was derived from surveys on Oct. 14 or Nov. 16. The surfzone width (L_{sz}) is the distance between the shoreline (x_{sl}, where alongshore-averaged water depth, $\langle h\rangle_y = 0$) and the beginning of wave breaking (x_{sz}).

Sim.	Time of Obs. (EDT)	Bathymetry	$\langle\eta\rangle$ (m)	H_s (m)	T_p (s)	θ (°)	σ_θ (°)	γ_J	L_{sz}
S1	Oct. 20 10:00	Oct. 14	-0.03	0.62	7.8	-3.4	30.8	1.9	70
S2	Oct. 20 15:00	Oct. 14	0.13	0.51	8.8	-15.0	29.5	1.8	58
S3a	Oct. 28 00:00	Oct. 14	-0.32	1.95	7.1	-2.1	28.6	1.4	146
S3b	Oct. 28 00:00	Nov. 16	-0.32	1.95	7.1	-2.1	28.6	1.4	134

2.3 Vorticity Wavenumber Spectra Analysis

The alongshore length scales of surfzone eddies are quantified with the hour average of 1-Hz alongshore wavenumber spectra of vertical vorticity (with the spatial mean removed) over the second hour of a simulation (3600 - 7200 s). The alongshore wavenumber spectra were computed from depth-averaged vertical vorticity ($S_{\omega\omega}$) and from vertical vorticity at individual elevations ($S_{\omega\omega}(z)$), for alongshore eddy length scales $L \geq 4$ m ($k/2\pi \leq 0.25$ m^{-1}, where k is the wavenumber) at each cross-shore grid location (2-m resolution). Vertical vorticity was estimated from gridded velocity components using a central-difference

297 approach [*Patankar*, 1980], where vorticity at individual vertical layers was computed from
298 horizontal velocities at time-evolving terrain-following sigma layers interpolated to a grid
299 of fixed elevations. To estimate phase-averaged vorticity, a 60-s moving average is applied
300 to the vertical vorticity prior to computing the wavenumber spectra of vertical vorticity at 1
301 Hz. The averaging is applied prior to, rather than following, the discrete vorticity estimate to
302 remove apparent instantaneous wave-induced vorticity that is an artifact of the discretization.

303 Wavenumber spectra were computed for the energetic shore-normal waves (S3a) over
304 the observed alongshore-variable bathymetry (measured Oct. 14, Figure 1a,c, $\sigma_{y,sz} = 0.86$
305 m) and for four additional simulations (Table 2) with the same forcing as in S3a (Table 1),
306 but with altered alongshore bathymetric variability and wave directional spread. The sen-
307 sitivity of eddy length scales to the incident wave field (*e.g.,* short-crested wave breaking)
308 is investigated with two simulations with the observed Oct. 14 bathymetry and with half of
309 the observed (S4, $\sigma_\theta = 14.3°$) and zero (S5) offshore directional spread. The influence of
310 alongshore bathymetric variability on the distribution of eddy length scales is addressed with
311 two simulations (S6, S7) with the observed offshore directional spread ($\sigma_\theta = 28.6°$) and
312 reduced alongshore bathymetric variability. S6 has bathymetry with half of the observed
313 alongshore variability ($\sigma_{y,sz} = 0.43$ m, bathymetric features decreased by half the observed
314 amplitude about the alongshore mean bathymetry, Figure 1c, right vertical bar), and S7 has
315 alongshore-uniform bathymetry set to the alongshore-average of the observed bathymetric
316 profiles ($\sigma_{y,sz} = 0$ m, Figure 1c, thick black curve).

317 **Table 2.** Simulations for the eddy length-scale analysis with the corresponding alongshore bathymetry stan-
318 dard deviation in the surf zone ($\sigma_{y,sz}$), and the offshore directional spread (σ_θ). All other model parameters
319 for each run are consistent with those for S3a (Table 1).

Sim. No.	$\sigma_{y,sz}$ (m)	σ_θ (°)
S3a	0.86	28.6
S4	0.86	14.3
S5	0.86	0
S6	0.43	28.6
S7	0	28.6

2.4 Very Low-Frequency Velocity Analysis

The very low-frequency (VLF) surfzone currents, defined here as currents in the band $0.003 < f < 0.007$ Hz, were computed with 1-Hz time series along several cross-shore transects of the three-dimensional SWASH simulations. Similar to the vorticity estimates at specific elevations, horizontal velocities at sigma layers were interpolated to a fixed vertical grid spanning from near the mean sea-surface to near the bed. Velocities defined as 'near-surface' are at the grid point closest to one half of the alongshore-averaged significant wave height below the mean sea-surface elevation. Velocities defined as 'near-bottom' are at the grid point closest to 0.03 m above the bed, typically outside of a surface-gravity wave bottom boundary layer. Temporal velocity spectral analyses were performed using a Hanning window period of 512 s with an overlap period of 256 s for a 1-hr cross- (u) and alongshore (v) velocity 1-Hz time series, yielding a $\Delta f = 0.002$ Hz with the lowest bin centered at $f = 0.002$ Hz and 28 DOF. To test the confidence in VLF statistics over the last hour of the 2-hr simulation, simulation S3a and S7 (Table 2 were run for a longer time period (4 hrs with 84 DOF). The statistics from the last hour of the 2-hr simulation (3600 - 7200 s) were similar to statistics from the last 3 hrs of the 4-hr simulation (3600 - 14400 s), justifying that the results are statistically significant for the shorter simulation. When converted to equivalent velocity using the linear finite-depth dispersion relationship, sea-surface elevation spectral levels ($S_{\eta\eta} * g/h$ where g is gravitational acceleration and h is mean water depth) within the VLF band are 1 to 2 orders of magnitude lower than the velocity spectral levels ($S_{uu} + S_{vv}$, *e.g.,* modeled at x, y = 132, 740 m in Figure 2, dashed lines indicate the VLF band), indicating that VLF motions are rotational rather than directly forced by sea, swell, or infragravity waves [*Lippmann et al.*, 1999; *MacMahan et al.*, 2010; *Elgar et al.*, 2019]. The observed and modeled velocity spectral levels at x, y = 132, 740 m are similar for infragravity and VLF motions (within the 95% confidence interval).

The VLF spectral densities (S_{uu}, S_{vv}) are computed as the sum of the frequency bins centered at $f = 0.004$ and 0.006 Hz. The squared coherence of the VLF velocity (λ_u^2, λ_v^2) and the phase relative to the near-surface VLF velocity (ϕ_u, ϕ_v, positive and negative phase indicate leading and lagging surface velocities) are computed as the energy weighted average over the $f = 0.004$ and 0.006 Hz bins [*Hannan*, 1970; *Priestely*, 1981]. To represent the relative variability of VLF velocities over the water column, $(u_{rms} - u_{0,rms})/u_{0,rms}$ and $(v_{rms} - v_{0,rms})/v_{0,rms}$, the normalized difference between the root mean square (rms) over time of filtered VLF velocities (u_{rms}, v_{rms}) and the near-surface velocity ($u_{0,rms}, v_{0,rms}$),

was computed from the band-passed 0.003 < f < 0.007 Hz) velocities [PL64 filter, *Rosenfeld*, 1983], where greater and less than 0 indicates more and less VLF velocity variance at depth relative to near the surface, respectively.

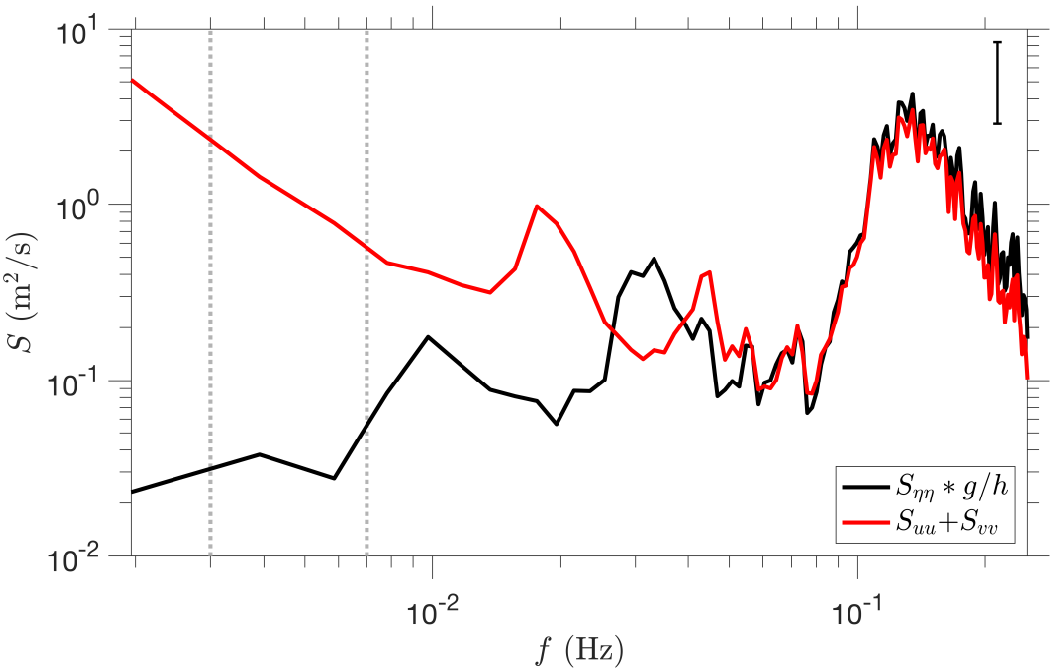

Figure 2. Sea-surface elevation spectral density converted to equivalent velocity ($S_{\eta\eta} * g/h$, black) and the sum of the depth-averaged cross- and alongshore spectral densities (S_{uu}, S_{vv}, red) in the surf zone (x, y = 132, 740 m) versus frequency (f). Vortical motion is the dominant energy in the VLF band (between the vertical dashed lines). The vertical bar indicates the 95% confidence interval for 28 DOF.

3 Results

3.1 Observed and Modeled Nearshore Conditions

The capability of SWASH to simulate surfzone circulation on a natural beach is tested by comparing modeled with the observed hourly bulk wave and current statistics. At the model offshore boundary (h = 11 m) for simulations with Oct. 14 bathymetry (S1, S2, S3a, Table 1) the alongshore-averaged $S_{\eta\eta}$ is similar to the observed sea-surface elevation spectra ($S_{\eta\eta}$, Figure 3, black curves). The observed and modeled $S_{\eta\eta}$ also are similar at h = 6 m (Figure 3, red curves), with slightly lower energy in the modeled spectra at the peak frequency for lower-energy waves (S1, S2). The differences between the observed and modeled spectra at h = 6 m may be associated with differences in the observed and modeled off-

shore spectrum and boundary conditions (Figure 3, black curves), including the assumption of uniform wave forcing along the offshore boundary, and inaccuracy in modeled physics (*e.g.,* wave transformation, wave-wave interactions, and other nonlinear processes).

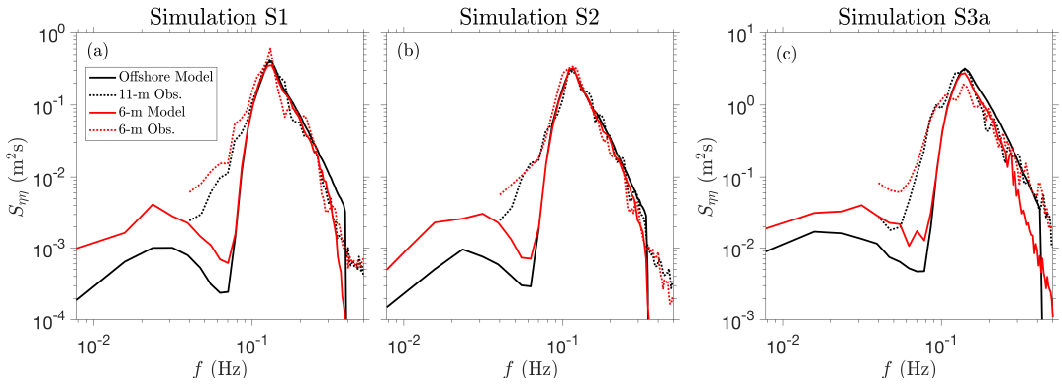

Figure 3. Sea-surface elevation spectral densities ($S_{\eta\eta}$) versus frequency (f) for alongshore-averaged model spectra at the offshore boundary (solid-black curves), observed spectra in 11-m depth (dashed-black curves), and simulated (solid-red curves) and observed (dashed-red curves) spectra in 6-m depth for simulations (a) S1, (b) S2, and (c) S3a. There are 48 DOF in the spectra.

The modeled and observed H_s for simulations with Oct. 14 bathymetry (S1, S2, S3a) have similar patterns, including a reduction in H_s from depth-limited breaking in the surf zone (Figure 4b,d, 5b, x_{sz}: white dashed lines) and smaller H_s near the pier due to wave refraction (around y = 500 m). Although the model simulates the observed cross-shore pattern of H_s, the modeled H_s is larger than observed (RMSE = 0.28 m, bias = 0.23 m, Figure 4b,d, 5b, colors in circles are darker than in the surrounding area). The positive bias of the modeled H_s is smaller if the stations near the pier (p84 and p85), where large changes in bathymetry may occur, are not included in the comparison (RMSE=0.21 m, bias = 0.18 m). The similar patterns and positive bias of modeled H_s relative to observations is shown along the cross-shore transect at y = 741 m (along stations p21-24, Figure 6a), where the modeled statistics are alongshore-averaged over 90 m ($696 \leq y \leq 786$ m, Figure 6, solid curves). A simulation with higher spatial resolution (1-m) performed for the same conditions as S1 resulted in similar errors between the modeled and observed wave height and velocities. Errors in H_s are larger than results from 3D simulations with small alongshore bathymetric variability [*Rijnsdorp et al.*, 2015], whereas the absolute biases are similar to 2-layer simulations at this field site [*Gomes et al.*, 2016]. The wave breaking parameters, α and β (Appendix A) were set to standard values from the literature and were not tuned to this dataset. Although

dissipation due to wave breaking may be improved with higher resolution simulations, increasing the number of vertical layers leads to instabilities. Due to the bathymetric uncertainty and a focus on understanding circulation dynamics rather than accurate hindcasting, tuning of the vertical resolution to minimize errors between the observed and modeled H_s was not investigated here.

The observed and simulated hour-averaged velocities include strong offshore-directed cross-shore velocities, $\langle u \rangle$, as part of bathymetric rip-current circulation cells, and alongshore velocities, $\langle v \rangle$, that meander around prominent bathymetric features with weaker $\langle v \rangle$ in the center of circulation cells (*e.g.,* y = 741 m, Figure 4a,c, 5a). The modeled depth-averaged velocities are on average higher than the observed velocities (bias = 0.04 m/s), but almost always are within the alongshore range (Figure 6, shaded regions, comparisons with depth-varying velocities at the instrument elevations are similar). For small shore-normal wave conditions (S1), the modeled and observed velocities have similar magnitudes with small differences that may be owing to localized bathymetric variability not resolved by the surveys or to migration of bathymetric features after the Oct. 14 survey (Figure 6b,c). For the moderate-energy shore-normal wave condition (S3a), the strongest modeled $\langle u \rangle$ appear to be shifted in the positive alongshore direction relative to the observations (Figure 5a), which may be due to migration of bathymetric features resulting from strong alongshore currents between Oct. 14 and Oct. 28.

To determine the sensitivity of the H_s and hour-averaged velocity spatial patterns to bathymetric variability, an additional simulation was conducted with bathymetry from Nov. 16 and the moderate-energy shore-normal wave conditions observed on Oct. 28 (S3b, same wave conditions as S3a). Oct 28 is approximately halfway between the dates of two bathymetry surveys (Figure 1a,b). The modeled $S_{\eta\eta}$ at h = 6 m is not sensitive to the survey bathymetry, but surfzone H_s are smaller in S3b than in S3a, and thus are more similar to observations (S3a: bias = 0.40 m, S3b: bias = 0.23 m, Figure 6d, compare black with red curves). In S3b, the position of the modeled circulation features, including the strong offshore-directed velocities, is similar to that of the observations, leading to smaller errors in a point-to-point comparison (S3a: RMSE = 0.30 m/s, S3b: RMSE = 0.13 m/s, Figure 6e,f).

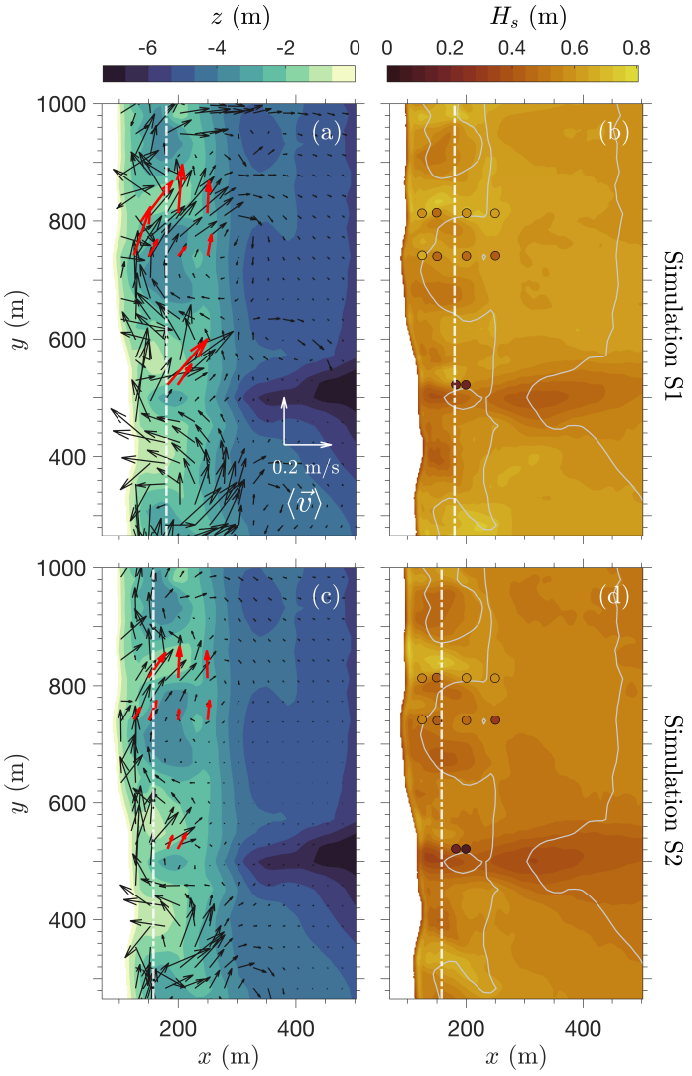

Figure 4. Observed (left: red arrows, right: filled circles) and modeled (left: black arrows, right: color contours) (a,c) hour-averaged depth-averaged velocity, $\langle\vec{v}\rangle$ and (b,d) significant wave height, H_s for small shore-normal (S1, a,b) and oblique (S2, c,d) wave conditions. Bathymetry (left: color contours, right: grey contour curves at 2.5 and 5.0 m depths) and the approximate outer edge of the surf zone (x_{sz}, all panels: dashed white lines) are shown. Sensor measurements that were removed during quality control are not included here.

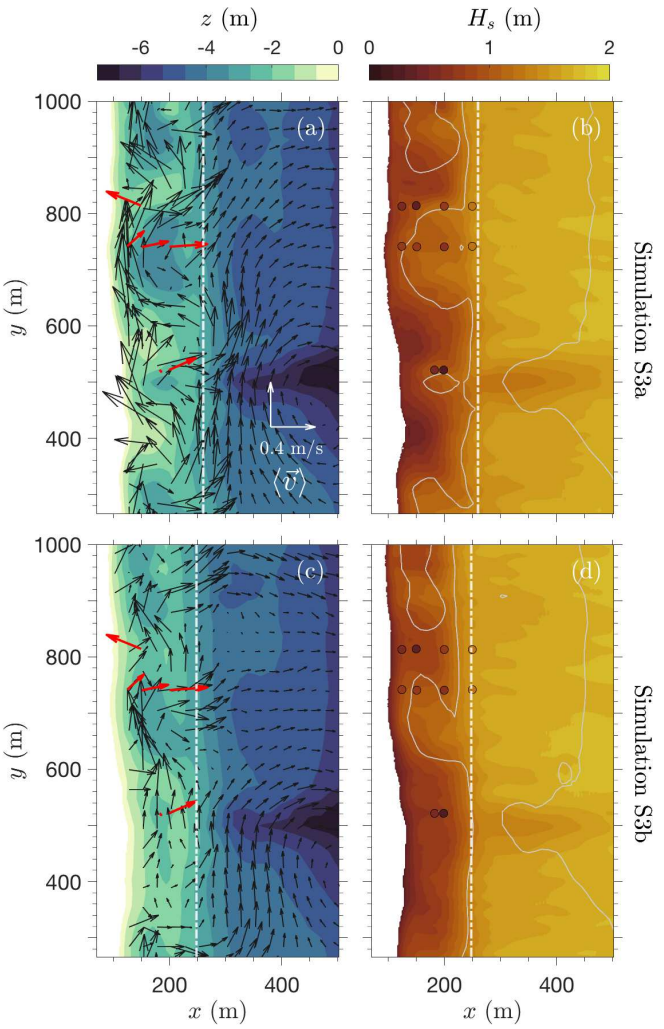

Figure 5. Observed (left: red arrows, right: filled circles) and modeled (left: black arrows, right: color contours) (a,c) hour-averaged depth-averaged velocity, $\langle \vec{v} \rangle$ and (b,d) significant wave height, H_s for moderate-energy shore-normal wave conditions on Oct. 28 with Oct. 14 (S3a, a,b) and Nov. 16 (S3b, c,d) bathymetry. Bathymetry (left: color contours, right: grey contour curves at 2.5 and 5.0 m depth) and the approximate outer edge of the surf zone (x_{sz}, all panels: dashed white lines) are shown. The $\langle \vec{v} \rangle$ scale (left) and H_s colorbar (right) span approximately twice the range of those in Figure 4.

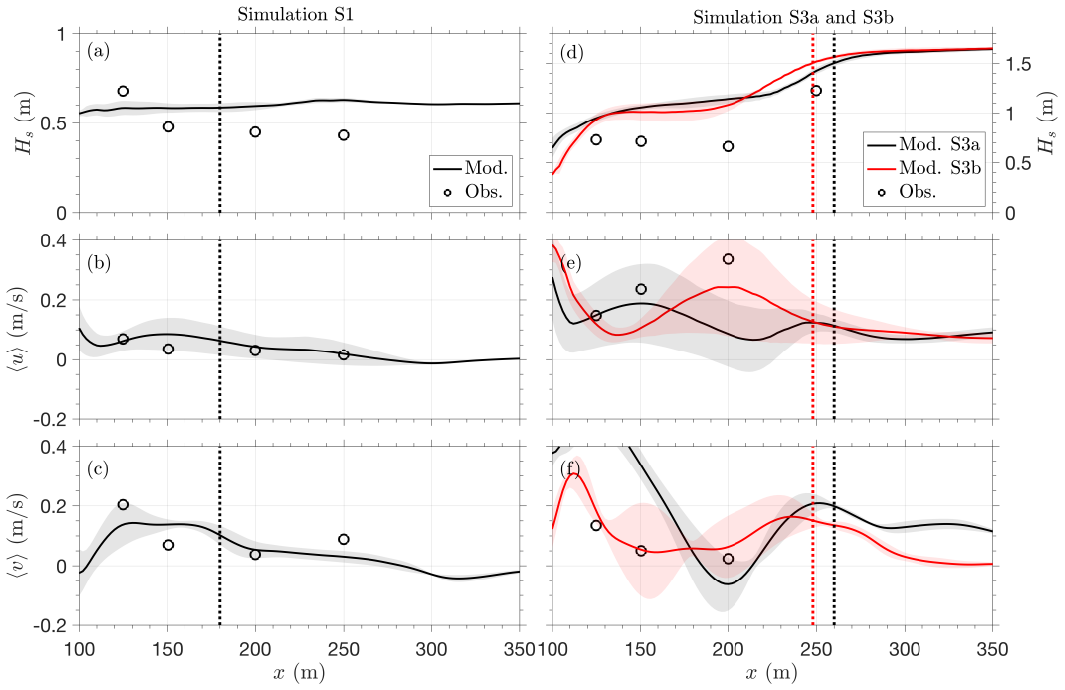

Figure 6. (a,d) Observed (circles) and modeled (curves) significant wave height, H_s and (b,e) 1-hr mean cross-shore, $\langle u \rangle$ and (c,f) alongshore $\langle v \rangle$ velocities along the cross-shore transect at $y = 741$ m (Figure 1) for simulations S1 (left), S3a (right, black), and S3b (right, red). Model results are represented as the cross-shore profiles of 90 m alongshore-averaged (curves) and standard deviation (shaded areas) of wave and current statistics. The black (S1, S3a) and red (S3b) dashed vertical lines are the alongshore-averaged outer edge of the surf zone, x_{sz}.

3.2 Vorticity Wavenumber Spectra

The cross-shore and vertical variability of eddy length scales on alongshore-variable bathymetry is not known. Here, the alongshore wavenumber spectra of the modeled vertical vorticity is considered for shore-normal waves (H_s = 2 m) with different directional spreads (S3a, S4, S5) and alongshore bathymetric variability (S3a, S6, S7, Table 2). The cross-shore coordinate is normalized by the surfzone width, L_{sz} (Table 1), where $L_{\mathrm{sz}} = x_{sz} - x_{sl}$, where x_{sz} is the position of the outer edge of the surf zone, and x_{sl} is the alongshore-mean position of the still-water shoreline. Swashzone dynamics, including strong runup and backwash velocities, along an alongshore-varying shoreline may dominate the vorticity field near and in the swash zone ($0L_{\mathrm{sz}} < x - x_{sl} < 0.2L_{\mathrm{sz}}$) and are not shown here, where the focus is on the inner ($0.2L_{\mathrm{sz}} < x - x_{sl} < 0.5L_{\mathrm{sz}}$) and outer surf zones ($0.5L_{\mathrm{sz}} < x - x_{sl} < 1.0L_{\mathrm{sz}}$), and just offshore of the surf zone ($1.0L_{\mathrm{sz}} < x - x_{sl} < 1.5L_{\mathrm{sz}}$).

3.2.1 Cross-Shore Variability of the Alongshore Wavenumber Spectra of Vorticity

For simulations conducted with observed Oct. 14 bathymetry ($\sigma_{y,\mathrm{sz}}$ = 0.86 m) and different offshore directional spreads (S3a, S4, S5), the magnitude of $S_{\omega\omega}$ is largest at large length scales ($L > 100$ m) and is insensitive to directional spread in the inner surf zone (Figure 7a). In contrast, in the outer surf zone and immediately outside the surf zone, $S_{\omega\omega}$ has more variance at large length scales for simulations with less directional spread (Figure 7b,c). The magnitude of $S_{\omega\omega}$ at small length scales ($O(10)$m), hypothesized to be associated with injection of vorticity from finite-crested breaking waves, is highest for the largest wave directional spread (S3a) at all cross-shore positions (Figure 7, top row). For the simulation with the largest directional spread (S3a, $\sigma_\theta = 28.6°$), the magnitude of $S_{\omega\omega}$ at $L < 85$ m in the outer surf zone, where wave breaking is strong, is larger than the magnitude in the inner surf zone and just offshore of the surf zone (Figure 7, top row, compare solid curves at $L^{-1} > 10^{-2}$ m^{-1}).

For simulations with observed offshore directional spread ($\sigma_\theta = 28.6°$) and differing alongshore bathymetric variability (S3a, S6, S7, Table 2), the variance of vorticity fluctuations at large length scales ($L > 100$ m) increases with increasing alongshore bathymetric variability (Figure 7, bottom row). The largest sensitivity to bathymetry of the $S_{\omega\omega}$ magnitude at large length scales occurred in the inner surf zone (Figure 7d), where deep trough and terrace bathymetric features are present. In contrast, the variance of small length-scale eddies

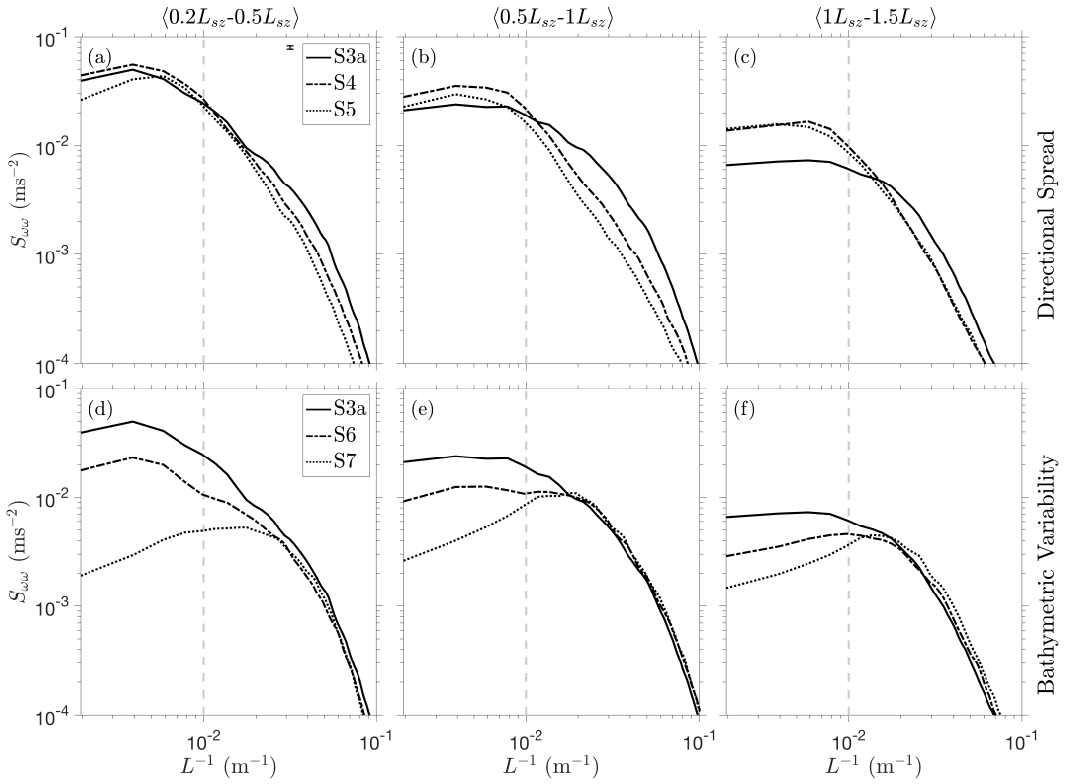

Figure 7. Cross-shore average of the alongshore wavenumber spectra of vorticity ($S_{\omega\omega}$) versus the inverse alongshore length scale (wavenumber divided by 2π, $L^{-1} = k_y/2\pi$), vertical dashed grey lines at $L = 100$ m) for (a,d) the inner surf zone ($0.2L_{\mathrm{sz}} < x - x_{sl} < 0.5L_{\mathrm{sz}}$), (b,e) the outer surf zone ($0.5L_{\mathrm{sz}} < x - x_{sl} < 1.0L_{\mathrm{sz}}$), and (c,f) just offshore of the surfzone edge ($1.0L_{\mathrm{sz}} < x - x_{sl} < 1.5L_{\mathrm{sz}}$) for (a-c) simulations with observed bathymetry and forced with large directional spread (S3a, $\sigma_\theta = 28.6°$, solid curves), half the directional spread (S4, $\sigma_\theta = 14.3°$, dot-dashed curves), and no directional spread (S5, $\sigma_\theta = 0°$, dotted curves), and for (d-f) simulations with directionally spread waves ($\sigma_\theta = 28.6°$) and observed Oct. 15 bathymetry (S3a, $\sigma_{y,sz} = 0.86$ m, solid curves), half the observed alongshore bathymetric variability (S6, $\sigma_{y,sz} = 0.43$ m, dot-dashed curves), and alongshore-averaged bathymetry (S7, $\sigma_{y,sz} = 0$ m, dotted curves). The vertical bar in (a) indicates the 95% confidence interval for 3540 DOF.

($O(10)$ m) is similar and relatively independent of alongshore bathymetric variability (Figure 7d-f).

3.2.2 Vertical Variability of the Alongshore Wavenumber Spectra of Vorticity

The cross-shore variability of eddy length scales has been investigated with models that account for the generation of eddies from short-crested wave breaking [*Kumar and Feddersen*, 2017; *O'Dea et al.*, 2020]. However, the vertical variability of eddy length scales is not known and has not been investigated using a three-dimensional phase-resolving model. Here, the alongshore wavenumber spectra of vertical vorticity at different elevations ($S_{\omega\omega}(z)$, computed with interpolated horizontal velocities, Section 2.3) are used to investigate the vertical variability of eddy length scales in the surf zone for shore-normal waves with Oct. 14 observed (S3a, Figure 8a-c) and alongshore-averaged (S7, Figure 8d-f) bathymetry. The magnitude of $S_{\omega\omega}(z)$ at large length scales ($L > 100$ m) is larger at all depths for the alongshore-varying (S3a) than for the alongshore-uniform (S7) bathymetry (compare Figure 8a-c with Figure 8d-f), consistent with the wavenumber spectra computed from the depth-averaged velocities ($S_{\omega\omega}$, Figure 7).

The magnitude of $S_{\omega\omega}(z)$ is nearly depth uniform outside of (not shown) and at the outer edge (Figure 8c,f) of the surf zone, and decays slightly with decreasing vertical elevations, primarily for small length-scale eddies, in the outer surf zone in both examples (Figure 8b,e) and in the inner surf zone for the alongshore uniform bathymetry (Figure 8d). The vertical dependence of $S_{\omega\omega}(z)$ in the inner surf zone for the alongshore-variable bathymetry is not evaluated here due to the inability to resolve $S_{\omega\omega}(z)$ at elevations that are below the seafloor at some alongshore locations (*e.g.,* $z < -0.75$ m at $0.5L_{\mathrm{sz}}$, Figure 8a). For the alongshore-variable bathymetry simulation (S3a), the vorticity variance (the area under $S_{\omega\omega}(z)$) for small eddy length scales (L$<$ 100 m) decays by 36% over 1 m in the water column in the outer surf zone (Figure 8b), whereas the vorticity variance for small length scales decreases by less than 15% over 2 m in the water column at the outer edge of the surf zone (Figure 8c). In the inner and outer surf zone for the alongshore-uniform bathymetry simulation (S7), the vorticity variance from near the surface ($z = -0.25$ m) to the lowest resolved elevation in the water column decays by $\geq$ 45% for small eddy length scales and $>$ 25% for large eddy length scales (Figure 8d,e).

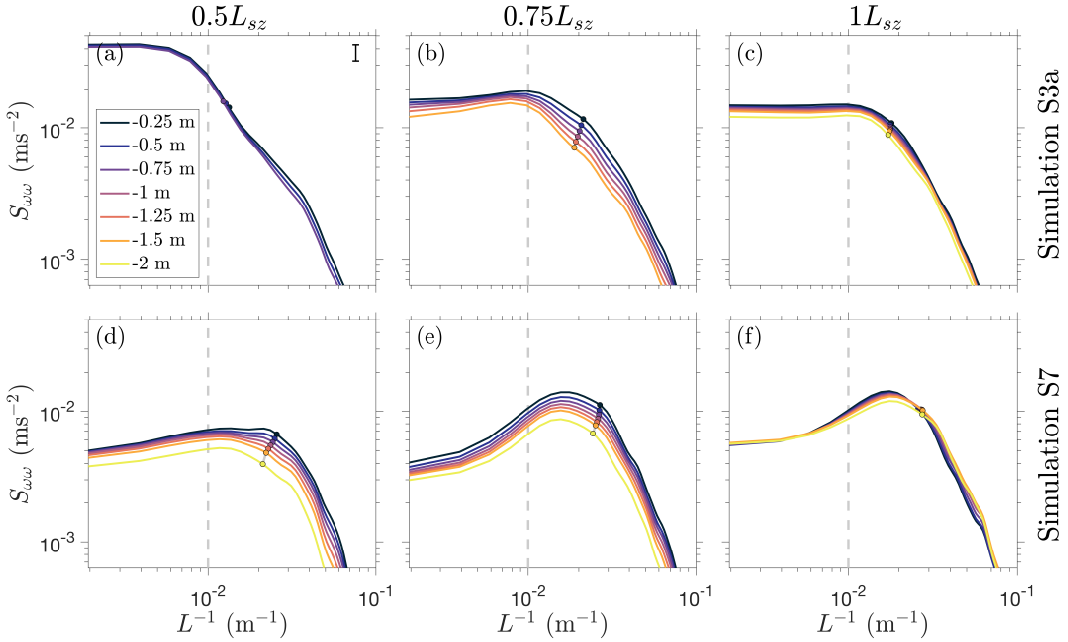

Figure 8. The alongshore wavenumber spectral density of vorticity ($S_{\omega\omega}(z)$) versus the inverse alongshore length scale (wavenumber divided by 2π, $L^{-1} = k_y/2\pi$), vertical dashed grey line at $L = 100$ m) for normalized cross-shore positions (a,d) in the inner surf zone ($x - x_{sl} = 0.5L_{sz}$), (b,e) the outer surf zone ($x - x_{sl} = 0.75L_{sz}$) and (c,f) the outer edge of the surf zone ($x - x_{sl} = 1.0L_{sz}$). At each location, the colored curves (legend inset, lighter curves nearer to the seafloor) are the spectra at 0.25 to 2 m below the mean sea-surface elevation for (a-c) observed bathymetry (S3a) and (d-f) alongshore-uniform bathymetry (S7). The circles (colored by elevation) are at the mean eddy length scale, $\overline{L}$ (centroid). The vertical bar (a) indicates the 95% confidence interval for 354 DOF.

Furthermore, the mean eddy length scale, $\overline{L}$ ($= \overline{k}_y/2\pi$, energy-weighted average length scale, the centroid of the spectrum, Figure 8 circles) of $S_{\omega\omega}(z)$ increases with decreasing vertical elevations in the surf zone for nearly all simulations (wavenumber decreases with decreasing vertical elevations, Figure 8b,d,e) and decreases or remains approximately the same over the vertical near the surfzone edge (Figure 8c,f) and just offshore of the surf zone (not shown). For the simulation with the observed bathymetry (S3a), $\overline{L}$ near-surface is $\sim$ 46 m and increases to $\sim$ 53 m over 1.25 m in the water column in the outer surf zone (Figure 8b). Similarly, for the alongshore-uniform bathymetry simulation (S7), $\overline{L}$ is $\sim$ 39 m near the surface and increases to $\sim$ 45 m over 1.5 m in the water column in the inner surf zone (Figure 8d).

3.3 Vertical Structure of Very Low-Frequency Motion

Field observations suggest there may be vertically varying structure of low-frequency eddies in the outer surf zone, but less variation in shallower depths [*Lippmann et al.*, 2016; *Henderson et al.*, 2017]. Here, the very low-frequency (VLF, $0.003 < f < 0.007$, Section 2.3, Figure 2) velocities from the simulation with moderate-energy shore-normal waves and Oct. 14 observed bathymetry (S3a, Figure 1) vary along the barred cross-shore profile (y = 741 m) and vertically in the outer surf zone (Figure 9). In the outer surf zone, the change in simulated cross-shore (alongshore) VLF velocities are up to 0.14 m/s (0.12 m/s) over the water column (not shown). The VLF velocity spectral density varies in the cross-shore, with the highest cross-shore VLF spectral density near the bar crest at $x = 220 - 240$ m (Figure 9a) and the highest alongshore VLF spectral density near the shoreline at $x < 100$ m (Figure 9e). The cross- and alongshore spectral densities are similar in magnitude at all locations, except near the bar crest where the cross-shore spectral density is much greater than the alongshore spectral density (Figure 9a,e). The coherence of VLF velocities at different elevations in the water column with those near the surface decreases with distance below the surface, including near the wave breaking region (around the bar crest, $x = 200 - 270$ m, Figure 9b,f). The VLF phase relative to the phase at the surface changes sign in the cross-shore (Figure 9c,g), indicating that near-bottom velocities alternate between leading and lagging surface velocities. The root-mean-squared (rms) VLF cross-shore velocities decrease with depth in the trough and near the bar crest ($x = 175 - 190$ and $x = 220 - 240$ m, Figure 9d), indicating more variable VLF velocities near the surface onshore of the onset of wave breaking.

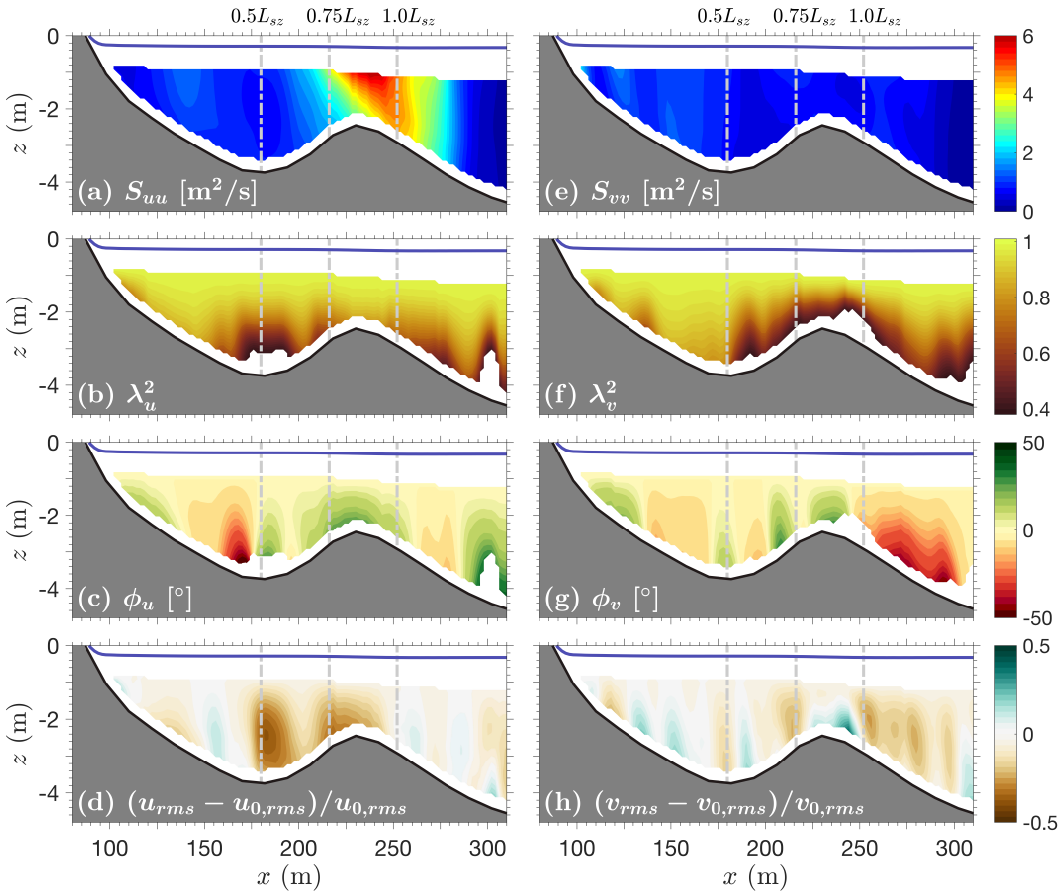

Figure 9. Cross-shore transect for the simulation S3a at y = 741 m of the (a-d) cross- and (e-h) alongshore VLF velocity spectral density (a: S_{uu}, e: S_{vv}), squared coherence (b: λ_u^2, f: λ_v^2), phase shift (c: ϕ_u, g: ϕ_v), and the normalized root-mean-squared (rms) difference (d: $(u_{rms} - u_{0,rms})/u_{0,rms}$, h: $(v_{rms} - v_{0,rms})/v_{0,rms}$) where negative (positive) indicates less (more) variability compared with the surface, with the mean sea-surface elevation (blue) and surfzone regions (dashed grey lines). Values are not shown for coherence squared and phase when the coherence is less than the 95% significance level.

The rms VLF alongshore velocities have relatively small vertical dependence onshore and offshore of the bar (Figure 9h).

Cross-shore transects at other regions of the S3a domain (*e.g.,* the terraced beach profile at $y \approx 850$ m, Figure 1) have similar vertical dependence in the outer surf zone (*e.g.,* $0.75L_{sz}$), as do VLF velocities with alongshore-uniform bathymetry (S7 simulation, not shown), suggesting that there is vertical variation of VLF velocities in the outer surf zone, with decreasing vertical dependence toward the shore for both the simulated alongshore-uniform and alongshore-varying bathymetry.

4 Discussion

4.1 Cross-Shore Variability of Vorticity Wavenumber Spectra

The length scales of horizontal eddies and their dependence on the incident wave forcing, coupled with the role of surfzone bathymetry, is a focus of recent studies [*Feddersen*, 2014; *Kumar and Feddersen*, 2017; *O'Dea et al.*, 2020]. Here, for simulations with varying offshore directional spread (σ_θ) on an alongshore inhomogeonous bathymetry, the vorticity variance, $\sigma^2_{\omega\omega}$ (the area under alongshore wavenumber spectra of depth-averaged vertical vorticity separated for inverse length scales (wavenumbers divided by 2π, $L^{-1} = k_y/2\pi$) on either side of 0.01 m^{-1}, $S_{\omega\omega}$, in Figure 7) at small length scales ($L < 100$ m) increases with directional spread in all cross-shore regions (Figure 10a, circles, squares, triangles, and linear fit with slopes = 3.2, 6.0, and 0.6×10^{-6} $m^{-1}s^{-2}$, respectively), consistent with results from previous modeling studies using a depth-integrated wave-resolving Boussinesq model with alongshore-uniform bathymetry [*Spydell and Feddersen*, 2009; *Suanda and Feddersen*, 2015] and alongshore-variable bathymetry [*O'Dea et al.*, 2020]. Multiple surfzone processes may contribute to the vorticity variance at small length scales, including generation by directionally spread short-crested breaking waves (*e.g.,* $\sigma_\theta = 28.6°$ in S3a). The small length-scale ($O(10)$ m) vorticity injected during wave breaking may be transferred to longer length scales through an inverse cascade [*Bühler and Jacobson*, 2001; *Boffetta and Ecke*, 2012; *Feddersen*, 2014; *Elgar et al.*, 2019; *Elgar and Raubenheimer*, 2020] or dissipated through bottom friction.

In contrast to small length scales, the dependence of large length-scale ($L > 100$ m) vorticity variance on directional spread differs by region within the surf zone, possibly owing to eddy coalescence and pulsations in mean circulation patterns. In the inner surf zone,

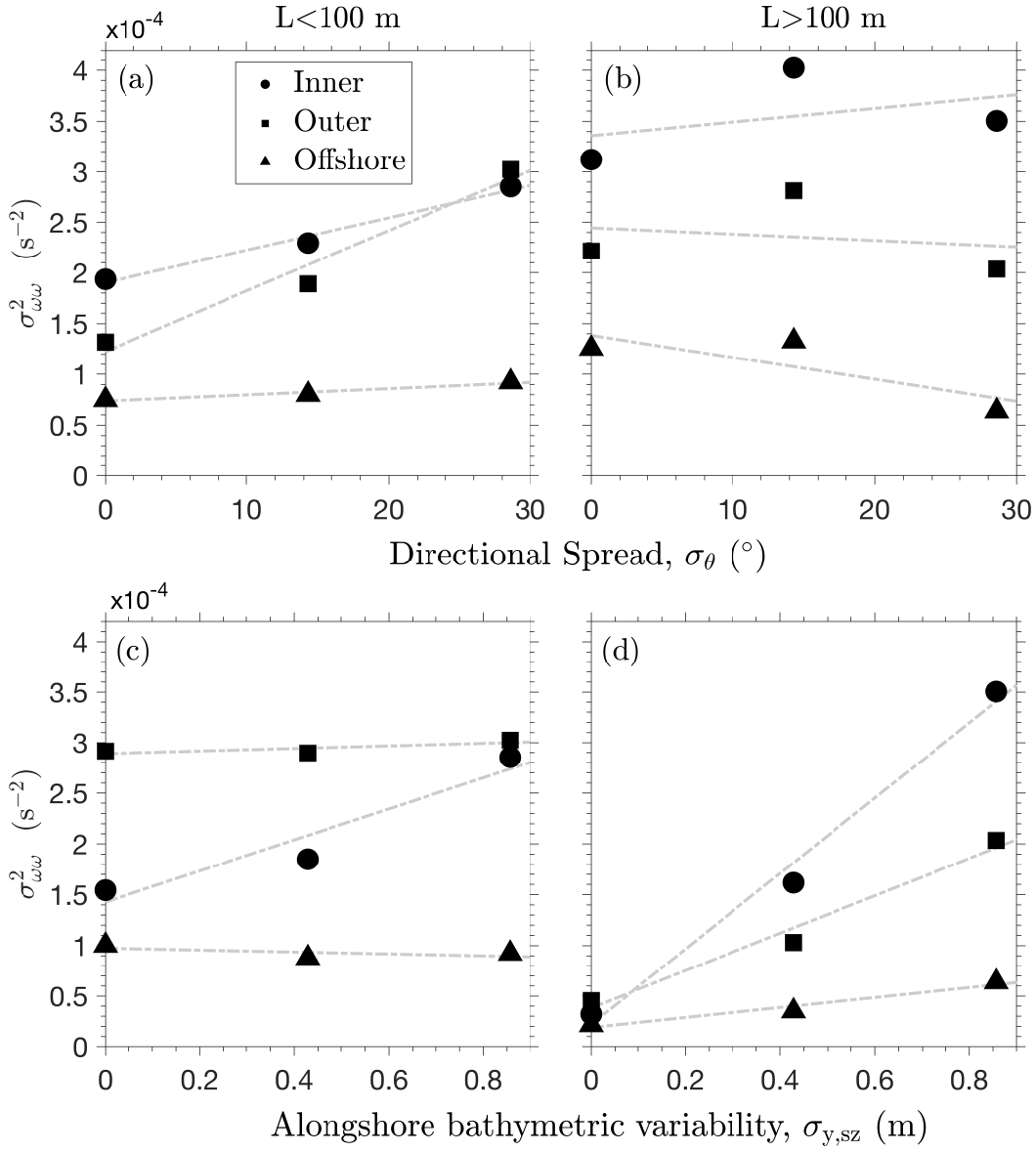

585 **Figure 10.** Vorticity variance, $\sigma^2_{\omega\omega}$ versus (a,b) directional spread, σ_θ (S3a, S4, S5) and (c,d) the stan-
586 dard deviation of surfzone bathymetric variability, $\sigma_{y,sz}$ (S3a, S6, S7) for (a,c) small (L<100 m) and (b,d)
587 large (L>100 m) eddy length scales for the inner (circles, $0.2L_{sz} < x - x_{sl} < 0.5L_{sz}$), outer (squares,
588 $0.5L_{sz} < x - x_{sl} < 1.0L_{sz}$), and offshore (triangles, $1.0L_{sz} < x - x_{sl} < 1.5L_{sz}$) of the surf zone. Linear
589 least-squares fits are given by the dashed-grey lines.

vorticity variance at large length scales are small and weakly increase with directional spread (Figure 10b, circles and linear fit with slope = 1.3×10^{-6} $m^{-1}s^{-2}$), possibly as a result of the enhancement of the coalescence of small length-scale eddies generated by short-crested wave breaking in the highly variable inner surf zone [*Bühler and Jacobson*, 2001; *Spydell and Feddersen*, 2009; *Clark et al.*, 2012] or fluctuations of strong inner surf zone circulation patterns (Figure 5a). In contrast, in the outer surf zone and just offshore of the surf zone, the vorticity variance at large length scales decreases with directional spread (Figure 10b, squares, triangles, and linear fit with slope = -0.6×10^{-6} $m^{-1}s^{-2}$ and -2.2×10^{-6} $m^{-1}s^{-2}$, respectively), which may result from fluctuations of strong mean circulation features that extend farther offshore for simulations with variable bathymetry and less directional spread [*O'Dea et al.*, 2020].

For simulations with a range of alongshore bathymetric variability (the maximum alongshore standard deviation of the seafloor elevation, $\sigma_{y,sz}$), the vorticity variance at small length scales ($L < 100$ m) is independent of bathymetric variability in the outer surf zone and just offshore of the surf zone (Figure 10c, triangles, squares, and linear fits with slopes = -0.2 and -0.1×10^{-4} $m^{-1}s^{-2}$, respectively), suggesting that small length-scale eddy generation is primarily a function of the incident wave field, rather than the surfzone bathymetric variability. However, in the inner surf zone, higher variance of medium length-scale ($L = 80 - 100$ m) eddies is present in the simulation with observed bathymetry ($\sigma_{y,sz} = 0.86$ m) than in simulations with less alongshore variability (Figure 7d, 10c). The source of this additional variance is unknown, but may be related to instabilities of the mean circulation, which tend to have moderate to long length scales associated with the bathymetric variability [*Tabeling et al.*, 1990; *Akkermans et al.*, 2008; *Geiman and Kirby*, 2013].

In contrast to the vorticity variance at small length scales, which is not strongly dependent on bathymetry, the eddy variance at large length scales ($L >$100 m) increases with alongshore bathymetric variability in all regions, particularly in the inner surf zone (Figure 10d, circles and linear fit with slope = 5.0×10^{-4} $m^{-1}s^{-2}$). There is a weaker increase in eddy variance with bathymetric variability in the outer surf zone and offshore of the surf zone (Figure 10d, squares, triangles, and linear fit with slopes = 2.5 and 0.7×10^{-4} $m^{-1}s^{-2}$, respectively). The role of bathymetric variability in controlling surfzone vorticity at large spatial scales, shown here as a function of the cross-shore position in the surf zone and degree of alongshore bathymetric variability, is consistent with previous findings that compared the

625 average variance across the entire surf zone for alongshore-uniform and alongshore-variable
626 bathymetry [*O'Dea et al.*, 2020].

627 The correlation of large-scale eddies with alongshore bathymetric variability, in con-
628 trast to no correlation with directional spread, suggests that bathymetric variability influ-
629 ences large-scale low-frequency fluctuations in the surf zone, possibly owing to enhanced
630 eddy interaction and coalescence in depressions or troughs (Figure 1a) [*Bühler and Jacob-*
631 *son*, 2001]. In addition, the highly variable observed bathymetry modulates wave breaking
632 patterns, driving meandering mean currents (Figure 5a), which may pulsate at low frequen-
633 cies and may shed large eddies [*MacMahan et al.*, 2004; *Reniers et al.*, 2007]. Eddy kinetic
634 energy is intensified in the surf zone in simulations with bathymetric variability [*Uchiyama*
635 *et al.*, 2017; *O'Dea et al.*, 2020]. Elevated eddy kinetic energy also is present outside of the
636 surf zone, where oscillations in bathymetrically driven circulation patterns [*e.g.,* rip current
637 jets, *Smith and Largier*, 1995; *Haller and Dalrymple*, 2001] or ejections of surfzone eddies
638 [*Feddersen*, 2014] may result in higher variance at large eddy length scales.

639 **4.2 Vertical Variability of the Vorticity Wavenumber Spectra**

640 Although previous studies have quantified surfzone eddy variability with alongshore
641 arrays of electromagnetic current meters at one elevation in the water column [*Oltman-Shay*
642 *et al.*, 1989; *Noyes et al.*, 2004], the depth variability of eddies in the surf zone has been in-
643 vestigated in only a few studies, and no previous numerical modeling experiments have in-
644 vestigated the vertical variability of vortical motion with a fully three-dimensional phase-
645 resolving model. Simulations with phase-averaged models have shown vertical structure of
646 shear instabilities [*Newberger and Allen*, 2007a,b] and the effect of vortex tilting on the sur-
647 fzone vorticity budget [*Uchiyama et al.*, 2017]. However, these models do not include wave-
648 forced eddy generation, which is an important source of eddy energy and may influence the
649 vertical structure of eddies [*Zhao et al.*, 2003; *Newberger and Allen*, 2007a].

650 Here, the energy levels of the alongshore wavenumber spectra of the simulated vertical
651 vorticity decrease slightly from the surface to the seafloor, particularly for small length-scale
652 eddies, and the mean eddy length scales (centroids of the spectra) increase (Figure 8, circles)
653 in some locations in the nearshore for all simulations, indicating that eddies may exhibit ele-
654 vation dependence for beaches with uniform or alongshore-varying bathymetry. The change
655 in magnitude and mean length scale of $S_{\omega\omega}(z)$ with location within the water column may

be related to length-scale dependent attenuation and the combined effects of bottom boundary layer dynamics, vertical mixing, and the vertical distribution of shear instabilities [*Zhao et al.*, 2003; *Boffetta and Ecke*, 2012; *Lippmann and Bowen*, 2016], which could result in depth variation of eddy stretching and tilting, as seen in three-dimensional phase-averaged ROMS simulations [*Uchiyama et al.*, 2017]. The vertical dependence of $S_{\omega\omega}(z)$ may be sensitive to changes in the vertical eddy viscosity [*Lippmann and Bowen*, 2016] and the incorporation of wave breaking related turbulence production [*Feddersen and Trowbridge*, 2005].

Simulations with alongshore-uniform bathymetry exhibit vertical variation at all length scales, whereas simulations with alongshore-variable bathymetry only have vertical variation in the outer surf zone (compare Figure 8a-c with Figure 8d-f), indicating that bathymetric variability may play a role in reducing the vertical dependence of large length-scale eddies. Although there is some vertical variation of eddies at all length-scales on alongshore uniform beaches (Figure 8d,e), on beaches with alongshore varying bathymetry the vertical dependence at small length scales decreases somewhat in the outer surf zone (Figure 8b) and is negligible in the inner and outer edge of the surf zone (Figure 8a,c). Thus, whereas small length-scale eddies may exhibit vertical dependence in the outer surf zone on beaches with large alongshore variability, larger length-scale eddies may be nearly depth-uniform on alongshore variable bathymetry.

4.3 Vertical Structure of Very Low-Frequency Motion

The three-dimensionality of very low-frequency (VLF) currents, which may impact material exchange and dispersion, is not well documented. Similar to the small number of observations of VLF motion vertical structure [*Lippmann et al.*, 2016; *Henderson et al.*, 2017], VLF motion simulated with SWASH varies in the vertical near the bar crest (Figure 9). Cross-shore energy density decays with depth, with over an 60% drop in squared coherence over the water column, and with large phase shifts near the bottom (up to 50°) relative to near-surface velocities [*Lippmann et al.*, 2016]. Simulated VLF velocities have weak vertical dependence of VLF motions near the outer edge of the surf zone with little vertical variation in shallower depths, broadly consistent with observations [*Lippmann et al.*, 2016; *Henderson et al.*, 2017].

Here, the simulated VLF motion exhibits vertical dependence in the outer surf zone, (*e.g.,* immediately onshore of the bar crest, $0.75L_{sz}$, Figures 8b, 9), with decreasing vertical

dependence toward the inner surf zone. Furthermore, simulated VLF velocities are elevation dependent for the terraced profile of S3a at $y \approx 850$ m (not shown), and for alongshore uniform bathymetry (S7, not shown). A theoretical model for eddy vertical dependence for a scenario with a depth-uniform alongshore mean current, constant eddy viscosity, no incorporation of surface sheer stresses from wave breaking, and varying bottom friction [*Lippmann and Bowen*, 2016] suggests the vertical structure of eddies in the surf zone may result from instabilities and bottom boundary layer dynamics. These solutions, which include bottom friction and linearized lateral momentum advection, suggest that eddy vertical structure may depend on vertical mixing, eddy scales, and the magnitude of shear in a mean alongshore current, but do not address shear in the cross-shore current or the role of variability in wave forcing in a phase-resolved framework.

The analyses here build on previous studies to investigate surfzone eddy dynamics by examining the alongshore length scales at lower frequencies than surface gravity waves [*Spydell and Feddersen*, 2009; *O'Dea et al.*, 2020] and cross-shore profiles of VLF flows ($0.003 < f < 0.007$ Hz) [*Lippmann et al.*, 2016; *Henderson et al.*, 2017]. The vertical dependence of $S_{\omega\omega}(z)$ and VLF horizontal velocities is largest in the outer surf zone ($0.75L_{sz}$, Figures 8b,e, 9), and decreases toward the shoreline. Near $0.5L_{sz}$, the coherence with near-surface cross-shore flows decreases toward the seafloor (Figure 9b), whereas it was not possible to fully assess the vertical dependence of the alongshore eddy length scales at $0.5L_{sz}$ for the alongshore variable bathymetry because the varying water depths preclude computing $S_{\omega\omega}(k)$ for $z < 0.75$ m. The vertical dependence of $S_{\omega\omega}(k)$ and VLF velocities may be influenced by vertical eddy viscosity, bottom drag, and absence of breaking-wave-generated turbulence in SWASH simulations. Although simulations suggest that low-frequency motions are primarily two-dimensional with some vertical structure, additional observational and numerical studies are necessary to understand the complex three-dimensional structure of VLF velocities in the surf zone, including the sensitivity of VLF velocities to wave conditions and surfzone bathymetries, and the implications for cross-shore exchange.

5 Conclusions

Simulations with a three-dimensional phase-resolving model (SWASH) reproduce the observed trends in wave transformation and the spatial patterns and magnitudes of the mean alongshore currents and meandering circulation on a barred beach with alongshore-inhomogeneous bathymetry. However, circulation features were sometimes shifted spatially

relative to the observations, and the simulated significant wave height was overestimated in the surf zone. The simulated surfzone circulation was sensitive to the bathymetry, which evolved during the field study.

The modeled dynamics include the horizontal and vertically-dependent structure of vortical motion in the surf zone. The alongshore eddy length scales were quantified using the alongshore wavenumber spectra of depth-averaged vorticity for simulations with different wave directional spreads and alongshore bathymetric variability. The variance of small length-scale eddies ($O(10)$ m) increases with directional spread and is independent of alongshore bathymetric variability in the outer surf zone and just offshore of the surf zone, suggesting that vortical motion with short alongshore length scales may be related to the incident wave field, and in particular to forcing by short-crested wave breaking, consistent with previous findings [*Spydell and Feddersen*, 2009; *Suanda and Feddersen*, 2015]. The variance of large length-scale eddies ($O(100)$ m) increases with alongshore bathymetric variability, indicating that alongshore bathymetric variability may intensify the formation of large length-scale eddies, in agreement with Bousinessq simulations with variability bathymetry [*O'Dea et al.*, 2020]. The variance of large length-scale eddies decreases with increasing directional spread in the outer surf zone and just offshore of the surf zone, suggesting that the relationship between directional spread and large length-scale eddies is not well understood, but may be related to instabilities in the stronger mean circulation in cases with less directional spread.

Modeled eddy length scales and low-frequency horizontal velocities were primarily two-dimensional with weak dependence on elevation in the outer surf zone, and occasionally in the inner surf zone for both uniform and alongshore-variable bathymetry. The magnitude of the alongshore wavenumber spectra of vorticity decreased, specifically at small length scales, and the mean length scale (spectral centroid) increased between the surface and the seafloor within the surf zone, whereas the vertical variation at the edge of the surf zone and just outside of the surf zone was small. The horizontal and vertical structures of very low-frequency (VLF) motions have complex patterns, including large drops in coherence and changes in phase between near-surface and subsurface flows. The vertical dependence of VLF velocities decreases from the outer surf zone toward the shoreline, broadly consistent with previous field studies [*Lippmann et al.*, 2016; *Henderson et al.*, 2017]. Further investigation is necessary to understand the complex three-dimensional vertical and horizontal variability of low-frequency motions in the surf zone.

Acknowledgments

We thank the staff of the USACE Field Research Facility, Duck, NC and of the PVLAB at the Woods Hole Oceanographic Institution for helping deploy, maintain, and recover sensors, for providing data from long-term sensors, and for bathymetric surveys. Also, we thank Pieter Smit for assistance with the model setup, and Jim Thomson, Falk Fedderson, and other reviewers for useful comments on the manuscript. Support was provided by the University of Washington Royalty Research Fund, the National Science Foundation, the Office of Naval Research, a National Defense Science and Engineering Graduate Fellowship, a Vannevar Bush Faculty Fellowship, the United States Army Corps of Engineers, the United States Coastal Research Program, Sea Grant, and the WHOI Investment in Science Program.

6 Data Availability Statement

Nearshore ADV data used in this study are available at `Zenodo-url-in-prep` (data archiving on Zenodo is underway; for review, the data is uploaded temporarily as Supporting Information) and bathymetry, water levels, and offshore wave data are provided by the USACE at `https://frfdataportal.erdc.dren.mil/`. Model configuration files, MATLAB processing codes, and model output used to produce figures in this paper are available at `https://doi.org/10.5281/zenodo.4141219`.

7 Appendix

A: Model description

Simulating WAves till SHore (SWASH) is based on an explicit, second-order finite difference method for horizontally staggered grids, and conserves mass and momentum at discrete levels for an incompressible fluid with a constant density, which enables an efficient scheme to simulate individual wave propagation and breaking with high spatio-temporal resolution [*Zijlema and Stelling*, 2005; *Zijlema et al.*, 2011]. The momentum equations are

$$\frac{\partial u_i}{\partial t} + \frac{\partial u_i u_j}{\partial x_j} = -\frac{1}{\rho}\frac{\partial p_h + p_{nh}}{\partial x_i} + \frac{\partial \tau_{ij}}{\partial x_j} - g\delta_{i3} \tag{A.1}$$

and

$$\frac{\partial u_j}{\partial x_j} = 0 \tag{A.2}$$

where x and u are the position and velocity in a Cartesian coordinate system ($i, j = 1, 2, 3$). Here, t is time, ρ is density, g is gravitational acceleration, τ_{ij} are turbulent stresses, and p_h (p_{nh}) is hydrostatic, $\rho g z$ (non-hydrostatic, $\rho g(\eta - z)$) pressure components. The time evolu-

780 tion of the surface elevation is determined by continuity,

$$\frac{\partial \eta}{\partial t} + \frac{\partial}{\partial x_i} \int_{-h}^{\eta} u_i dz = 0 \tag{A.3}$$

781 where h is the stationary bottom boundary, η is the moving free-surface, and z is the verti-
782 cal coordinate ($x_{i=3}$). The surface and bottom kinematic boundary layers constrain particle
783 motion, providing the constraints at the fixed bottom,

$$w|_{z=-h} = -u_i \frac{\partial h}{\partial x_i} \tag{A.4}$$

784 and the free-surface,

$$w|_{z=\eta} = \frac{\partial \eta}{\partial t} + u_i \frac{\partial \eta}{\partial x_i} \tag{A.5}$$

785 where w is the vertical velocity ($u_{i=3}$) and there is a constant pressure ($p_h = p_{nh} = 0$) and
786 no surface stresses at the free-surface. The bottom boundary shear stress, τ_b is based on a
787 quadratic friction law, with the drag coefficient, c_f determined from the Manning-Strickler
788 formulation such that

$$c_f = 0.015(k/h)^{1/3} \tag{A.6}$$

789 where k is the Nikuradse roughness height, set as 1 mm, within the range of values used in
790 previous studies at this cite [*Hsu et al.*, 2006].

791 The turbulent stresses are obtained from a turbulent viscosity approximation ($\tau_{xx} =$
792 $\upsilon_h \frac{\partial u}{\partial x}$, where υ_h is the horizontal eddy viscosity and $\tau_{xz} = \upsilon_v \frac{\partial u}{\partial z}$, where υ_v is the vertical
793 eddy viscosity) [*Smit et al.*, 2013; *Rijnsdorp et al.*, 2017]. The horizontal eddy viscosity is
794 approximated with the Smagorinksy model with a Smagorinsky constant of 0.1 [*Smagorin-*
795 *sky*, 1963], and vertical mixing is approximated using the $k - \epsilon$ model, with k the turbulent
796 kinetic energy per unit mass and ϵ the dissipation rate of turbulent kinetic energy per unit
797 mass [*Launder and Spalding*, 1983]. The vertical eddy viscosity allows for diffusion of this
798 stress into the water column, including coupling between vertical layers, and also increases
799 numerical stability [*Smit et al.*, 2013]. A 10^{-3} m^2/s background eddy viscosity was speci-
800 fied to account for unresolved vertical mixing, enhancing stability in the model. This value is
801 small compared with the vertical viscosity computed by the standard $k - \epsilon$ model. Although
802 the breaking-induced turbulence is not directly implemented in SWASH, model simulations
803 have shown that the turbulent kinetic energy below spilling breakers is well predicted [*Rijns-*
804 *dorp et al.*, 2017].

The simulation stability was improved further by discretization with flux-limited (shock-resolving) vertical advective terms indicated with the first-order upwind scheme. At points where velocity is computed, the water depths are approximated with the Monotonic Upstream-centered Scheme for Conservation Laws limiter (MUSCL), a finite volume method that improves numerical accuracy. Non-hydrostatic pressure gradients in the vertical momentum equations are approximated with the Keller-box scheme [*Lam and Simpson*, 1976]. Explicit time integration is performed using a specified Courant number between 0.05 and 0.30, and the vertical time integration uses the implicit Euler Scheme.

SWASH simulates wave breaking using a hydrostatic front approximation, similar to disabling dispersive terms in the Boussinesq equations [*Tissier et al.*, 2012; *Tonelli and Petti*, 2010], by prescribing a hydrostatic pressure distribution in the model around the discontinuity of a breaking wave. The turbulent wave-front is regarded as a sub-grid flow feature where the vertical accelerations are not resolved and the non-hydrostatic pressure is set to zero. The hydrostatic front approximation is initiated when local surface steepness exceeds a fraction of the shallow water celerity,

$$\frac{\partial \eta}{\partial x} > \alpha \sqrt{gh} \tag{A.7}$$

where α is a parameterized value. The spatial persistence of wave breaking is achieved by labeling a mesh-point for hydrostatic computation if the neighboring grid point has been labelled for hydrostatic computation and the local steepness exceeds a fraction of the shallow water celerity (Equation A.7) where the parameterized value is replaced with a coefficient β. In all simulations, wave breaking is controlled with a threshold parameter for initiation of wave breaking at a mesh-point, $\alpha = 0.6$ [*Lynett Patrick J.*, 2006] and for the neighboring mesh-points, $\beta = 0.3$. This approach, combined with the conservation of momentum, leads to appropriate levels of energy dissipation on the front face of a breaking wave [*Peregrine*, 1983].

References

Akkermans, R., A. Cieslik, L. Kamp, R. Trieling, H. Clercx, and G. Van Heijst (2008), The three-dimensional structure of an electromagnetically generated dipolar vortex in a shallow fluid layer, *Physics of Fluids*, *20*(11), 116,601.

Allen, J. S., P. A. Newberger, and R. A. Holman (1996), Nonlinear shear instabilities of alongshore currents on plane beaches, *Journal of Fluid Mechanics*, *310*, 181–213, doi:

10.1017/S0022112096001772.

Apotsos, A., B. Raubenheimer, S. Elgar, and R. Guza (2008), Wave-driven setup and alongshore flows observed onshore of a submarine canyon, *Journal of Geophysical Research: Oceans*, *113*(C7).

Boehm, A. B., N. S. Ismail, L. M. Sassoubre, and E. A. Andruszkiewicz (2017), Oceans in Peril: Grand Challenges in Applied Water Quality Research for the 21st Century, *Environmental Engineering Science*, *34*(1), 3–15, doi:10.1089/ees.2015.0252.

Boehm, F. R., L. Sandrini-Neto, T. Moens, and P. da Cunha Lana (2016), Sewage input reduces the consumption of rhizophora mangle propagules by crabs in a subtropical mangrove system, *Marine environmental research*, *122*, 23–32.

Boffetta, G., and R. E. Ecke (2012), Two-Dimensional Turbulence, *Annual Review of Fluid Mechanics*, *44*(1), 427–451, doi:10.1146/annurev-fluid-120710-101240.

Bowen, A. J., and R. A. Holman (1989), Shear instabilities of the mean longshore current: 1. Theory, *Journal of Geophysical Research: Oceans*, *94*(C12), 18,023–18,030, doi:10.1029/JC094iC12p18023.

Bowen, A. J., D. L. Inman, and V. P. Simmons (1968), Wave 'set-down' and set-Up, *Journal of Geophysical Research*, *73*(8), 2569–2577, doi:10.1029/JB073i008p02569.

Bühler, O., and T. E. Jacobson (2001), Wave-driven currents and vortex dynamics on barred beaches, *Journal of Fluid Mechanics*, *449*, 313–339, doi:10.1017/S0022112001006322.

Castelle, B., T. Scott, R. Brander, and R. McCarroll (2016), Rip current types, circulation and hazard, *Earth-Science Reviews*, *163*, 1–21.

Clark, D. B., F. Feddersen, and R. T. Guza (2010), Cross-shore surfzone tracer dispersion in an alongshore current, *Journal of Geophysical Research: Oceans*, *115*(C10), doi:10.1029/2009JC005683.

Clark, D. B., F. Feddersen, and R. T. Guza (2011), Modeling surf zone tracer plumes: 2. Transport and dispersion, *Journal of Geophysical Research: Oceans*, *116*(C11), doi:10.1029/2011JC007211.

Clark, D. B., S. Elgar, and B. Raubenheimer (2012), Vorticity generation by short-crested wave breaking, *Geophysical Research Letters*, *39*(24), doi:10.1029/2012GL054034.

Dalrymple, R. A., J. H. MacMahan, A. J. Reniers, and V. Nelko (2011), Rip Currents, *Annual Review of Fluid Mechanics*, *43*(1), 551–581, doi:10.1146/annurev-fluid-122109-160733.

de Bakker, A. T. M., M. F. S. Tissier, and B. G. Ruessink (2016), Beach steepness effects on nonlinear infragravity-wave interactions: A numerical study, *Journal of Geophysical Research: Oceans*, *121*(1), 554–570, doi:10.1002/2015JC011268.

Derakhti, M., J. T. Kirby, F. Shi, and G. Ma (2016), Nhwave: Consistent boundary conditions and turbulence modeling, *Ocean Modelling*, *106*, 121–130.

Elgar, S., and B. Raubenheimer (2020), Field evidence of inverse energy cascades in the surf zone, *Journal of Physical Oceanography*.

Elgar, S., B. Raubenheimer, and R. T. Guza (2005), Quality control of acoustic Doppler velocimeter data in the surfzone, *Measurement Science and Technology*, *16*(10), 1889–1893, doi:10.1088/0957-0233/16/10/002.

Elgar, S., B. Raubenheimer, D. B. Clark, and M. Moulton (2019), Extremely Low Frequency (0.1 to 1.0 mHz) Surf Zone Currents, *Geophysical Research Letters*, *46*(3), 1531–1536, doi:10.1029/2018GL081106.

Feddersen, F. (2012), Scaling surf zone turbulence, *Geophysical Research Letters*, *39*(18).

Feddersen, F. (2014), The Generation of Surfzone Eddies in a Strong Alongshore Current, *Journal of Physical Oceanography*, *44*(2), 600–617, doi:10.1175/JPO-D-13-051.1.

Feddersen, F., and J. Trowbridge (2005), The effect of wave breaking on surf-zone turbulence and alongshore currents: A modeling study, *Journal of Physical Oceanography*, *35*(11), 2187–2203.

Feddersen, F., R. T. Guza, S. Elgar, and T. H. C. Herbers (1998), Alongshore momentum balances in the nearshore, *Journal of Geophysical Research: Oceans*, *103*(C8), 15,667–15,676, doi:10.1029/98JC01270.

Feddersen, F., D. B. Clark, and R. T. Guza (2011), Modeling surf zone tracer plumes: 1. Waves, mean currents, and low-frequency eddies, *Journal of Geophysical Research*, *116*(C11), doi:10.1029/2011JC007210.

Garcez-Faria, A. F., E. B. Thornton, T. P. Stanton, C. V. Soares, and T. C. Lippmann (1998), Vertical profiles of longshore currents and related bed shear stress and bottom roughness, *Journal of Geophysical Research: Oceans*, *103*(C2), 3217–3232, doi:10.1029/97JC02265.

Garcez-Faria, A. F., E. B. Thornton, T. C. Lippmann, and T. P. Stanton (2000), Undertow over a barred beach, *Journal of Geophysical Research: Oceans*, *105*(C7), 16,999–17,010, doi:10.1029/2000JC900084.

Geiman, J. D., and J. T. Kirby (2013), Unforced Oscillation of Rip-Current Vortex Cells, *Journal of Physical Oceanography*, *43*(3), 477–497, doi:10.1175/JPO-D-11-0164.1.

Gomes, E. R., R. P. Mulligan, K. L. Brodie, and J. E. McNinch (2016), Bathymetric control on the spatial distribution of wave breaking in the surf zone of a natural beach, *Coastal Engineering*, *116*, 180–194, doi:10.1016/j.coastaleng.2016.06.012.

Guza, R. T., and E. B. Thornton (1980), Local and shoaled comparisons of sea surface elevations, pressures, and velocities, *Journal of Geophysical Research: Oceans*, *85*(C3), 1524–1530, doi:10.1029/JC085iC03p01524.

Haller, M. C., and R. A. Dalrymple (2001), Rip current instabilities, *Journal of Fluid Mechanics*, *433*, 161–192, doi:10.1017/S0022112000003414.

Haller, M. C., U. Putrevu, J. Oltman-Shay, and R. A. Dalrymple (1999), Wave group forcing of low frequency surf zone motion, *Coastal engineering journal*, *41*(02), 121–136.

Hally-Rosendahl, K., and F. Feddersen (2016), Modeling surfzone to inner-shelf tracer exchange, *Journal of Geophysical Research: Oceans*, *121*(6), 4007–4025, doi:10.1002/2015JC011530.

Hannan, E. (1970), Multiple time series, *Wiley*, p. 536.

Hansen, J. E., B. Raubenheimer, J. H. List, and S. Elgar (2015), Modeled alongshore circulation and force balances onshore of a submarine canyon, *Journal of Geophysical Research: Oceans*, *120*(3), 1887–1903.

Henderson, S. M., J. Arnold, H. T. Özkan-Haller, and S. A. Solovitz (2017), Depth Dependence of Nearshore Currents and Eddies, *Journal of Geophysical Research: Oceans*, *122*(11), 9004–9031, doi:10.1002/2016JC012349.

Hsu, T.-J., S. Elgar, and R. Guza (2006), Wave-induced sediment transport and onshore sandbar migration, *Coastal Engineering*, *53*(10), 817–824.

Kraichnan, R. H. (1967), Inertial Ranges in Two-Dimensional Turbulence, *The Physics of Fluids*, *10*(7), 1417–1423, doi:10.1063/1.1762301.

Kuik, A., G. P. Van Vledder, and L. Holthuijsen (1988), A method for the routine analysis of pitch-and-roll buoy wave data, *Journal of physical oceanography*, *18*(7), 1020–1034.

Kumar, N., and F. Feddersen (2017), The Effect of Stokes Drift and Transient Rip Currents on the Inner Shelf. Part I: No Stratification, *Journal of Physical Oceanography*, *47*(1), 227–241, doi:10.1175/JPO-D-16-0076.1.

Kumar, N., G. Voulgaris, J. C. Warner, and M. Olabarrieta (2012), Implementation of the vortex force formalism in the coupled ocean-atmosphere-wave-sediment transport (COAWST) modeling system for inner shelf and surf zone applications, *Ocean Modelling*, *47*, 65–95, doi:10.1016/j.ocemod.2012.01.003.

Lam, D. C. L., and R. B. Simpson (1976), Centered differencing and the box scheme for diffusion convection problems, *Journal of Computational Physics*, *22*(4), 486–500, doi: 10.1016/0021-9991(76)90045-0.

Launder, B. E., and D. B. Spalding (1983), The numerical computation of turbulent flows, in *Numerical prediction of flow, heat transfer, turbulence and combustion*, pp. 96–116, Elsevier.

Lentz, S. J., and M. R. Fewings (2012), The wind-and wave-driven inner-shelf circulation, *Annual review of marine science*, *4*, 317–343.

Lippmann, T. C., and A. J. Bowen (2016), The Vertical Structure of Low-Frequency Motions in the Nearshore. Part II: Theory, *Journal of Physical Oceanography*, *46*(12), 3713–3727, doi:10.1175/JPO-D-16-0015.1.

Lippmann, T. C., T. H. C. Herbers, and E. B. Thornton (1999), Gravity and Shear Wave Contributions to Nearshore Infragravity Motions, *Journal of Physical Oceanography*, *29*(2), 231–239, doi:10.1175/1520-0485(1999)029<0231:GASWCT>2.0.CO;2.

Lippmann, T. C., E. B. Thornton, and T. P. Stanton (2016), The Vertical Structure of Low-Frequency Motions in the Nearshore. Part I: Observations, *Journal of Physical Oceanography*, *46*(12), 3695–3711, doi:10.1175/JPO-D-16-0014.1.

Long, J. W., and H. T. Özkan Haller (2009), Low-frequency characteristics of wave group–forced vortices, *Journal of Geophysical Research*, *114*(C8), doi:10.1029/2008JC004894.

Longuet-Higgins, M. S. (1970), Longshore currents generated by obliquely incident sea waves: 1, *Journal of Geophysical Research (1896-1977)*, *75*(33), 6778–6789, doi: 10.1029/JC075i033p06778.

Longuet-Higgins, M. S., and R. w. Stewart (1964), Radiation stresses in water waves; a physical discussion, with applications, *Deep Sea Research and Oceanographic Abstracts*, *11*(4), 529–562, doi:10.1016/0011-7471(64)90001-4.

Lynett Patrick J. (2006), Nearshore Wave Modeling with High-Order Boussinesq-Type Equations, *Journal of Waterway, Port, Coastal, and Ocean Engineering*, *132*(5), 348–357, doi: 10.1061/(ASCE)0733-950X(2006)132:5(348).

MacMahan, J. H., A. J. H. M. Reniers, E. B. Thornton, and T. P. Stanton (2004), Infragravity rip current pulsations, *Journal of Geophysical Research: Oceans*, *109*(C1), doi:10.1029/2003JC002068.

MacMahan, J. H., E. B. Thornton, and A. J. H. M. Reniers (2006), Rip current review, *Coastal Engineering*, *53*(2), 191–208, doi:10.1016/j.coastaleng.2005.10.009.

MacMahan, J. H., A. J. H. M. Reniers, and E. B. Thornton (2010), Vortical surf zone velocity fluctuations with 0(10) min period, *Journal of Geophysical Research*, *115*(C6), C06,007, doi:10.1029/2009JC005383.

Moulton, M., S. Elgar, B. Raubenheimer, J. C. Warner, and N. Kumar (2017), Rip currents and alongshore flows in single channels dredged in the surf zone, *Journal of Geophysical Research: Oceans*, *122*(5), 3799–3816, doi:10.1002/2016JC012222.

Newberger, P. A., and J. S. Allen (2007a), Forcing a three-dimensional, hydrostatic, primitive-equation model for application in the surf zone: 2. Application to DUCK94, *Journal of Geophysical Research: Oceans*, *112*(C8), doi:10.1029/2006JC003474.

Newberger, P. A., and J. S. Allen (2007b), Forcing a three-dimensional, hydrostatic, primitive-equation model for application in the surf zone: 1. Formulation, *Journal of Geophysical Research: Oceans*, *112*(C8), doi:10.1029/2006JC003472.

Noyes, T. J., R. Guza, S. Elgar, and T. Herbers (2004), Field observations of shear waves in the surf zone, *Journal of Geophysical Research*, *109*(C1), doi:10.1029/2002JC001761.

O'Dea, A., N. Kumar, and M. Haller (2020), Simulations of the surf zone eddy field and cross-shore exchange on a non-idealized bathymetry, *Journal of Geophysical Research: Oceans*.

Oltman-Shay, J., P. A. Howd, and W. A. Birkemeier (1989), Shear instabilities of the mean longshore current: 2. Field observations, *Journal of Geophysical Research: Oceans*, *94*(C12), 18,031–18,042, doi:10.1029/JC094iC12p18031.

Patankar, S. V. (1980), Numerical heat transfer and fluid flow, hemisphere publ, *Corp., New York*, *58*.

Peregrine, D. (1998), Surf Zone Currents, *Theoretical and Computational Fluid Dynamics*, *10*(1), 295–309, doi:10.1007/s001620050065.

Peregrine, D. H. (1983), Water waves, nonlinear Schrödinger equations and their solutions, *The ANZIAM Journal*, *25*(1), 16–43, doi:10.1017/S0334270000003891.

Pineda, J., J. A. Hare, and S. Sponaugle (2007), Larval Transport and Dispersal in the Coastal Ocean and Consequences for Population Connectivity, *Oceanography*, *20*(3), 22–39.

Plant, N. G., K. T. Holland, and J. A. Puleo (2002), Analysis of the scale of errors in nearshore bathymetric data, *Marine Geology*, *191*(1), 71–86, doi:10.1016/S0025-3227(02)

998 00497-8.

999 Priestely, M. (1981), Spectral analysis and time series, *Academic Press*, p. 890.

1000 Putrevu, U., J. Oltman-Shay, and I. A. Svendsen (1995), Effect of alongshore nonuniformities
1001 on longshore current predictions, *Journal of Geophysical Research: Oceans*, *100*(C8),
1002 16,119–16,130, doi:10.1029/95JC01459.

1003 Raubenheimer, B., R. T. Guza, and S. Elgar (2001), Field observations of wave-driven set-
1004 down and setup, *Journal of Geophysical Research: Oceans*, *106*(C3), 4629–4638, doi:
1005 10.1029/2000JC000572.

1006 Reniers, A. J. H. M., E. B. Thornton, T. P. Stanton, and J. A. Roelvink (2004a), Vertical flow
1007 structure during Sandy Duck: observations and modeling, *Coastal Engineering*, *51*(3),
1008 237–260, doi:10.1016/j.coastaleng.2004.02.001.

1009 Reniers, A. J. H. M., J. A. Roelvink, and E. B. Thornton (2004b), Morphodynamic model-
1010 ing of an embayed beach under wave group forcing, *Journal of Geophysical Research:*
1011 *Oceans*, *109*(C1), doi:10.1029/2002JC001586.

1012 Reniers, A. J. H. M., J. H. MacMahan, E. B. Thornton, and T. P. Stanton (2007), Modeling
1013 of very low frequency motions during RIPEX, *Journal of Geophysical Research: Oceans*,
1014 *112*(C7), doi:10.1029/2005JC003122.

1015 Rijnsdorp, D. P., P. B. Smit, and M. Zijlema (2012), Non-hydrostatic modelling of infragrav-
1016 ity waves using swash, *Coastal Engineering Proceedings*, *1*(33), 27, doi:10.9753/icce.v33.
1017 currents.27.

1018 Rijnsdorp, D. P., P. B. Smit, and M. Zijlema (2014), Non-hydrostatic modelling of in-
1019 fragravity waves under laboratory conditions, *Coastal Engineering*, *85*, 30–42, doi:
1020 10.1016/j.coastaleng.2013.11.011.

1021 Rijnsdorp, D. P., G. Ruessink, and M. Zijlema (2015), Infragravity-wave dynamics in a
1022 barred coastal region, a numerical study, *Journal of Geophysical Research: Oceans*,
1023 *120*(6), 4068–4089, doi:10.1002/2014JC010450.

1024 Rijnsdorp, D. P., P. B. Smit, M. Zijlema, and A. J. H. M. Reniers (2017), Efficient non-
1025 hydrostatic modelling of 3d wave-induced currents using a subgrid approach, *Ocean Mod-*
1026 *elling*, *116*, 118–133, doi:10.1016/j.ocemod.2017.06.012.

1027 Rosenfeld, L. (1983), Code-1: Moored array and large-scale data report, *Woods Hole*
1028 *Oceanographic Institution Tech. Rep*, pp. 83–23.

1029 Ruessink, B., J. Miles, F. Feddersen, R. Guza, and S. Elgar (2001), Modeling the alongshore
1030 current on barred beaches, *Journal of Geophysical Research: Oceans*, *106*(C10), 22,451–

22,463.

Ruju, A., J. L. Lara, and I. J. Losada (2014), Numerical analysis of run-up oscillations under dissipative conditions, *Coastal Engineering*, *86*, 45–56, doi:10.1016/j.coastaleng.2014.01.010.

Shanks, A. L., S. G. Morgan, J. MacMahan, and A. J. H. M. Reniers (2010), Surf zone physical and morphological regime as determinants of temporal and spatial variation in larval recruitment, *Journal of Experimental Marine Biology and Ecology*, *392*(1), 140–150, doi:10.1016/j.jembe.2010.04.018.

Simons, R. R., T. J. Grass, and M. Mansour-Tehrani (1992), Bottom shear stresses in the boundary layers under waves and currents crossing at right angles, *Coastal Engineering Proceedings*, *1*(23), doi:10.9753/icce.v23.%p.

Smagorinsky, J. (1963), General circulation experiments with the primitive equations, *Monthly Weather Review*, *91*(3), 99–164, doi:10.1175/1520-0493(1963)091<0099:GCEWTP>2.3.CO;2.

Smit, P., M. Zijlema, and G. Stelling (2013), Depth-induced wave breaking in a non-hydrostatic, near-shore wave model, *Coastal Engineering*, *76*, 1–16, doi:10.1016/j.coastaleng.2013.01.008.

Smit, P., T. Janssen, L. Holthuijsen, and J. Smith (2014), Non-hydrostatic modeling of surf zone wave dynamics, *Coastal Engineering*, *83*, 36–48, doi:10.1016/j.coastaleng.2013.09.005.

Smith, J. A., and J. L. Largier (1995), Observations of nearshore circulation: Rip currents, *Journal of Geophysical Research: Oceans*, *100*(C6), 10,967–10,975.

Smith, J. M., S. Bak, T. Hesser, M. A. Bryant, and C. Massey (2017), Frf wave test bed and bathymetry inversion, *Coastal Engineering Proceedings*, *1*(35), 22, doi:10.9753/icce.v35.waves.22.

Spydell, M., and F. Feddersen (2009), Lagrangian Drifter Dispersion in the Surf Zone: Directionally Spread, Normally Incident Waves, *Journal of Physical Oceanography*, *39*(4), 809–830, doi:10.1175/2008JPO3892.1.

Stive, M. J. F., and H. G. Wind (1982), A study of radiation stress and set-up in the nearshore region, *Coastal Engineering*, *6*(1), 1–25, doi:10.1016/0378-3839(82)90012-6.

Stoner, N., and M. Dorfman (2007), Testing the waters: a guide to water quality at vacation beaches, *Natural Resources Defense Council*, *8*(2010), 12.

1063 Suanda, S. H., and F. Feddersen (2015), A self-similar scaling for cross-shelf exchange
1064 driven by transient rip currents, *Geophysical Research Letters*, *42*(13), 5427–5434, doi:
1065 10.1002/2015GL063944.

1066 Tabeling, P., O. Cardoso, and B. Perrin (1990), Chaos in a linear array of vortices, *Journal of*
1067 *Fluid Mechanics*, *213*, 511–530.

1068 Tissier, M., P. Bonneton, F. Marche, F. Chazel, and D. Lannes (2012), A new approach to
1069 handle wave breaking in fully non-linear Boussinesq models, *Coastal Engineering*, *67*,
1070 54–66, doi:10.1016/j.coastaleng.2012.04.004.

1071 Tonelli, M., and M. Petti (2010), Finite volume scheme for the solution of 2d extended
1072 Boussinesq equations in the surf zone, *Ocean Engineering*, *37*(7), 567–582, doi:10.1016/j.
1073 oceaneng.2010.02.004.

1074 Uchiyama, Y., J. C. McWilliams, and A. F. Shchepetkin (2010), Wave–current interaction in
1075 an oceanic circulation model with a vortex-force formalism: Application to the surf zone,
1076 *Ocean Modelling*, *34*(1), 16–35, doi:10.1016/j.ocemod.2010.04.002.

1077 Uchiyama, Y., J. C. McWilliams, and C. Akan (2017), Three-dimensional transient rip cur-
1078 rents: Bathymetric excitation of low-frequency intrinsic variability: 3-D TRANSIENT
1079 RIP CURRENTS, *Journal of Geophysical Research: Oceans*, *122*(7), 5826–5849, doi:
1080 10.1002/2017JC013005.

1081 Visser, P. J. (1986), Wave basin experiments on bottom friction due to current and waves,
1082 *Coastal Engineering Proceedings*, *1*(20), doi:10.9753/icce.v20.%p.

1083 Warner, J. C., B. Armstrong, R. He, and J. B. Zambon (2010), Development of a Coupled
1084 Ocean–Atmosphere–Wave–Sediment Transport (COAWST) Modeling System, *Ocean*
1085 *Modelling*, *35*(3), 230–244, doi:10.1016/j.ocemod.2010.07.010.

1086 Zhao, Q., I. A. Svendsen, and K. Haas (2003), Three-dimensional effects in shear waves,
1087 *Journal of Geophysical Research: Oceans*, *108*(C8), doi:10.1029/2002JC001306.

1088 Zijlema, M., and G. S. Stelling (2005), Further experiences with computing non-hydrostatic
1089 free-surface flows involving water waves, *International Journal for Numerical Methods in*
1090 *Fluids*, *48*(2), 169–197, doi:10.1002/fld.821.

1091 Zijlema, M., G. Stelling, and P. Smit (2011), SWASH: An operational public domain code
1092 for simulating wave fields and rapidly varied flows in coastal waters, *Coastal Engineering*,
1093 *58*(10), 992–1012, doi:10.1016/j.coastaleng.2011.05.015.